Detection and characterization of Earth's interior signals in geodetic data using blind source separation methods

Olivier de Viron, Michel van Camp, Nicolas Sidére

Geophys. J. Int. (2000) **142,** 000–000

Detection and characterization of Earth's interior signals in geodetic data using blind source separation methods

Olivier de Viron[1], Michel Van Camp[2], Nicolas Sidère[3]

[1] *LIENSs UMR7266 (La Rochelle University, CNRS),* [2] *Royal Belgian Institute of Natural Sciences,*

[3] *Laboratoire Informatique, Image, Interaction, La Rochelle University*

SUMMARY

We assess the potential of blind source separation (BSS) methods to recover signals originating from Earth's interior, using synthetic tests and satellite gravimetry data. Seven BSS methods are evaluated in terms of their ability to detect and characterize low-amplitude interior signals embedded in dominant noise and climate-induced variability. Our results show that detection is generally feasible even when interior signals have small relative amplitudes; in this context, classical Principal Component Analysis (PCA) provides the most reliable detection performance. However, detailed characterization of the spatial and temporal structure of the interior signal proves more challenging. Independent Component Analysis (ICA) offers improved characterization compared to other methods, but only when the interior signal's variability is comparable to that of climate signals. We then apply a two-step screening process to GRACE satellite gravity data. First, PCA is applied independently at each grid point across Earth's surface, successfully retrieving major climate signals previously identified in the literature. Second, we use PCA on an earthquake catalog spanning the GRACE observation period and find that earthquakes with magnitudes below 8.5 can be detected. However, the correlation between the retrieved components and earthquake-induced gravity signals remains too weak to support meaningful geophysical interpretation. These results highlight both the promise and the current limitations of BSS methods for investigating Earth's internal processes using space-based gravimetry.

Key words: Geodesy, Satellite gravity, Statistical methods.

1 INTRODUCTION

Among the various components of the global Earth observation system, geodesy – the science concerned with measuring the Earth's shape, gravity field, and spatial orientation – provides observations that are directly sensitive to the distribution of mass within the planet. Over several decades, geodetic measurements have yielded precise and valuable insights into the Earth system and its temporal evolution (Rummel, 2010; Sindoni et al., 2016). In particular, geodetic time series capture signals related to tectonic motions (Altamimi et al., 2016), glacial isostatic adjustment (GIA) (Métivier et al., 2020), and variations in water mass distribution associated with seasonal and climatic fluctuations (Gobron et al., 2021; Tapley et al., 2019). Additionally, geodetic data can reveal specific phenomena originating in the Earth's interior, such as co-, pre-, and post-seismic deformations, as well as volcanic activity and processes occurring in the core (Mandea et al., 2012; Panet et al., 2022; Saraswati et al., 2023).

Despite these advances, our knowledge of Earth's internal dynamics remains limited (Liu & Mao, 2021). Earthquakes, for example, are routinely detected and analyzed, yet they represent only one part of the seismic cycle, while other mass – or density – related processes associated with fault systems remain much less constrained (Fabbri et al., 2024). Similarly, geodetic data may contain information on a range of other internal processes – such as core flows, magmatic or volcanic activity, or dike intrusions – that are still poorly understood due to limited observational evidence (Alpala et al., 2025; Jin et al., 2013). The ability to identify and characterize such signals within noisy geodetic datasets is therefore of considerable geophysical importance.

Two broad lines of methodological research have emerged in the analysis of geodetic time series. One line emphasizes the detection of transient or anomalous behaviors in the data, often using realistic synthetic time series to assess the sensitivity and robustness of detection algorithms. Synthetic packages such as Fakenet, developed in the context of the Southern California Earthquake Center geodetic transient detection validation exercise, provide network-based simulations that enable systematic evaluation of methods designed to identify slow fault slip from spatially distributed geodetic observations (Agnew, 2013; Murray et al., 2013; Riel et al., 2014).

A second line of research uses geodetic observations from an entire monitoring network to reconstruct the underlying, time-dependent fault slip and deformation fields. Rather than merely detecting anomalous signals, these methods solve an inverse problem to identify the physical processes responsible for the observed surface displacements (Bekaert et al., 2016; Dmitrieva et al., 2015; Segall & Matthews, 1997).

However, these two approaches address fundamentally different questions. Detection-oriented studies aim at establishing whether a signal is present at all, whereas source separation methods are often implicitly expected to go one step further, namely to separate, reconstruct, and physically interpret the underlying sources.

This separation can be approached through three main methodological frameworks:

Explicit modeling: When the influence of one or several sources on the geodetic observables is precisely known, their effects can be explicitly modeled and subtracted from the data. Typical examples include tidal corrections (Van Camp et al., 2017) or the separation of core contributions from atmospheric effects in length-of-day variations (Holme & de Viron, 2013).

Joint analysis: When multiple observables respond to the same physical processes – such as changes in mass distribution – but with different sensitivities or transfer functions, their joint analysis can facilitate the separation of individual effects. For instance, Métivier et al. (2020) and Ziegler et al. (2022) combined GNSS with altimetry and gravimetry measurements to distinguish present-day ice melting from glacial isostatic adjustment.

Exploiting spatio-temporal structures: When the spatial and temporal behaviors of the contributing processes differ sufficiently, these differences can be exploited to separate their signatures. For example, distinct frequency characteristics allow the use of filtering techniques to isolate sources. Spatially distributed measurements of a single geodetic observable can be treated jointly to resolve the evolution of deformation or slip on faults using time-dependent network inversion methods (e.g. Dmitrieva et al., 2015; Murray et al., 2013; Segall & Matthews, 1997; Bekaert et al., 2016). Moreover, when the sources exhibit statistical independence in time, Blind Source Separation (BSS) methods can be applied to recover their individual contributions. Those BSS methods will be the focus of the present study.

Among BSS methods, Principal Component Analysis (PCA, (Preisendorfer & Mobley, 1988)) remains the most widely used in geodesy. It has been employed to reveal geophysical signals embedded in geodetic time series, including signals related to water mass redistribution (Hanjiang et al., 2009; Rangelova et al., 2007; Schmidt et al., 2008), glacial isostatic adjustment (GIA) (Scherneck et al., 2001), earthquake-related processes (Chao & Liau, 2019; Kositsky & Avouac, 2010; Munekane, 2012), and interannual climate variability (de Viron et al., 2006). PCA has also found application in noise reduction (Wouters & Schrama, 2007; Schrama et al., 2007), joint analysis of heterogeneous geodetic datasets (Crossley et al., 2012; Rangelova & Sideris, 2008; Zerbini et al., 2013), outlier detection (Magyar et al., 2022), and reconstruction of gravitational potential variations (Nerem et al., 2013).

Other BSS approaches have been explored in geodetic contexts, though to a lesser extent. For example, Independent Component Analysis (ICA, (Hyvärinen & Oja, 1999)) has been applied to synthetic scenarios (Forootan & Kusche, 2012) and satellite gravity data (Boergens et al., 2014; Forootan & Kusche, 2012; Forootan et al., 2012), for denoising purposes (Frappart et al., 2011), or to isolate specific signals of interest, such as earthquake signatures (Maubant et al., 2020; Xiong et al., 2024). Some studies have shown that ICA may outperform PCA for retrieving certain high-amplitude signals (Xiong et al., 2024, for example).

In practice, most geodetic applications of BSS rely on qualitative validation criteria: extracted components are deemed satisfactory because they resemble expected spatial or temporal patterns. Yet, in the absence of controlled synthetic tests, such visual agreement cannot guarantee that the separation is clean, that source mixing has been effectively removed, or that the reconstructed signal faithfully represents the true geophysical process. As a consequence, although BSS methods have demonstrated their usefulness as detection tools, their actual performance in terms of source separation and reconstruction accuracy remains largely unexplored in a systematic manner. This distinction between detecting a signal and reliably characterizing it is central to the present study.

The objective of this paper is to evaluate the capability of BSS methods to recover interior Earth signals that are obscured by stronger contributions from climatic processes. It extends the work of Forootan & Kusche (2012) by testing a broader range of BSS methods, with particular attention to the challenge posed by interannual climate variability, which often masks subtle endogeneous, i.e. Earth interior, geophysical signals (de Viron et al., 2008; Valty et al., 2015).

Specifically, this study aims to determine under which conditions a geophysical signal of internal origin – typically weak and masked by dominant climatic variability – can be detected by BSS methods, and under which conditions it can be faithfully reconstructed. Here, detection means that a recovered mode correlates with the target more strongly than in 95 % of cases where no endogenous geophysical signal is present; it is a statement about the null distribution, not about the fidelity of the reconstruction, whereas characterization implies a high-fidelity reconstruction, exhibiting strong spatial and temporal correlation with the true underlying geophysical process and minimal contamination from other sources. Importantly, as far as we know, no systematic assessment has yet been carried out regarding the precision and reliability of these methods when applied to geodetic data. We address this gap with synthetic tests. Unlike in the statistical literature, where analytical results can often be derived for idealized models, the diversity of geophysical signals and noise structures makes closed-form demonstrations intractable. Simulations, by giving full control over the source signals and their characteristics, allow us instead to span a wide range of scenarios and to quantify the conditions under which BSS methods succeed or fail.

Specifically, this study answers the following questions: (a) What is the minimum endogenous-to-climate signal ratio at which interior signals become detectable by BSS methods? And what ratio is required for their temporal evolution to be faithfully recovered? (b) Which parameters most influence the performance of blind detection and reconstruction? (c) Which BSS methods perform best in terms of signal separation? (d) What types of interior signals are most amenable to successful extraction?

Based on the results from the synthetic tests, Principal Component Analysis (PCA) emerges as the most effective method for detecting endogenous signals, while Independent Component Analysis (ICA) can, in certain configurations, provide a more accurate reconstruction of the endogenous signatures. This conclusion holds across a wide range of signal types representative of Earth's interior processes, but the reconstruction quality is found to be not precise enough for geophysical interpretation, except in simulations where the Earth interior signal to climate signal ratio is larger than one, and only if the number of sources is small.

To test our results on actual data, we applied PCA to the GRACE (Gravity Recovery And Climate Experiment) satellite gravity dataset. As with other geodetic observables, gravity data reflect a superposition of signals from various sources, including both climatic and solid Earth processes. However, since the true underlying geophysical signal is unknown in real data, there is no ground truth against which to assess reconstruction fidelity: we can therefore establish detection, but not compare the characterization performance of ICA relative to PCA in this context.

In the following sections, we first describe the methodology and synthetic experiment design used to evaluate the performance of different BSS methods. We then present and discuss the results of these synthetic tests, highlighting the relative strengths of PCA and ICA in various configurations. Finally, we demonstrate the application of PCA to real GRACE data to explore its practical utility in detecting signals from Earth's interior. For clarity, we refer hereafter to endogenous signals as those originating from the Earth's interior, in contrast with climate-related signals.

2 PROBLEM FORMULATION

In this study, we consider geodetic observations as the superposition of three main contributions: endogenous signals, climatic signals, and stochastic observational noise. At station ℓ and time t, the observed time series can be written as

$$D_\ell(t) \;=\; \sum_{j=1}^{J} g_{\ell j}\, G_j(t) \;+\; \sum_{k=1}^{K} c_{\ell k}\, C_k(t) \;+\; N_\ell(t), \tag{1}$$

where $G_j(t)$ represents endogenous sources (e.g., post-seismic transients, tectonic signals), $C_k(t)$ denotes external climate-related sources (e.g., hydrology mass distribution change, for example linked to climate modes such as ENSO, NAO,...), and $N_\ell(t)$ corresponds to random noise. The coefficients $g_{\ell j}$ and $c_{\ell k}$ are local amplitudes drawn from predefined distributions, reflecting the spatial variability of the sources.

The noise term is modeled as a combination of independent realizations of white and power-law processes, consistent with the stochastic properties of geodetic time series. Each realization $N_\ell(t)$ is generated independently across stations, so that this noise component is spatially incoherent by construction. We did not additionally introduce spatially coherent noise, since such a component would be statistically indistinguishable, in this framework, from an additional climate source, itself modeled as a power-law process with spatially correlated coefficients. The climate sources are taken from normalized climate indices, assumed to be independent of the endogenous sources. The endogenous signals are represented by simple parametric forms (e.g., Heaviside step, exponential decay, sine function), which capture the temporal behavior of typical solid Earth processes.

For simplicity, we assume that noise processes are uncorrelated with endogenous or climate signals, and that the sources $G_j(t)$ and $C_k(t)$ are statistically independent. Spatial and temporal dependencies are therefore separable: spatial correlations are expressed through the station-dependent coefficients $g_{\ell j}$ and $c_{\ell k}$, while temporal correlations arise from the functional forms of $G_j(t)$ and $C_k(t)$.

Our objective is to recover the endogenous sources $G_j(t)$ and the associated space patterns $g_{\ell j}$ from the observed mixtures $D_\ell(t)$. Two success criteria are considered:

- **Detection**, when the correlation between a retrieved source and the original endogenous signal exceeds the 95th percentile of correlations obtained under the null hypothesis (no endogenous signal; i.e., in simulations generated from Eq. (1) with $g_{\ell j} = 0$ for all j, meaning no endogenous contribution, with climate and noise sources unchanged);
- **Characterization**, when the correlation exceeds 0.8, corresponding to the retrieval of at least 64% of the variance of the original signal.

This formulation explicitly defines the statistical model underlying our experiments and provides the basis for evaluating BSS methods.

3 BLIND SOURCE SEPARATION METHODS

BSS methods aim to recover the original source signals from a set of observed time series that are assumed to be linear or nonlinear mixtures of these sources. To conduct a comprehensive evaluation of blind source separation (BSS) methods, we tested seven approaches. While only the first three – Principal Component Analysis, Independent Component Analysis, specifically Fast Independent Component Analysis, and Isometric Feature Mapping – proved effective in practice, we present all of them here in this section for completeness, highlighting their methodology, mathematical foundations, and applicability to source separation problems.

3.1 Principal Component Analysis (PCA)

3.1.1 Methodology

Principal Component Analysis (PCA), first introduced by Pearson (1901) and applied in a geophysical context in Savage (1988), is a classical technique for dimensionality reduction. In meteorology and oceanography, PCA is also known as Empirical Orthogonal Function (EOF) analysis. PCA transforms a set of possibly correlated variables into a smaller set of uncorrelated variables called *principal components* (PCs). This implies that the separation criterion is the orthogonality in time between the sources, as estimated from the covariance matrix of the time series.

These components are constructed to capture the directions of maximum variance in the data.

Given a centered dataset$\mathbf{D} \in \mathbb{R}^{n \times d}$ (with n samples and d variables), the sample covariance matrix is

$$\mathbf{\Sigma} = \frac{1}{n-1}\mathbf{D}^T\mathbf{D}.$$

The eigenvectors $\mathbf{v}_i$ and eigenvalues λ_i of $\mathbf{\Sigma}$ satisfy

$$\mathbf{\Sigma}\mathbf{v}_i = \lambda_i \mathbf{v}_i,$$

or, in the matrix form

$$\mathbf{\Sigma}\mathbf{V} = \mathbf{V}\Lambda,$$

with $\mathbf{V} = [\mathbf{v}_1, \ldots, \mathbf{v}_d]$, orthonormal, and $\Lambda = diag(\lambda_1 \geq ...\lambda_d-$. Projecting the data onto these directions yields the principal components, or scores, $\mathbf{Y} = \mathbf{DV}$. The columns of $\mathbf{V}$, which give the weights of the variables in each score, are conventionally called the loadings. The eigenvalues give the variance of the corresponding score, $\mathrm{var}Y_i = \lambda_i$, and $\lambda_i / \left(\sum_k \lambda_k\right)$ defines how much the eigen vector v_i, and the associated principal component, captures of the total variance of the signal.

In practice, most of the variance of $\mathbf{D}$ is often captured by the first few principal components (Fraino, 2023; von Storch & Zwiers, 1999). If the original dataset has d variables, we retain the k leading components with $k \ll d$ and project the data as

$$\mathbf{Y} = \mathbf{D}\mathbf{V}_k,$$

where $\mathbf{V}_k$ contains the k leading eigenvectors. The rows of $\mathbf{Y}$ are called the *scores*, i.e. the representation of each observation in the new k-dimensional space. This provides a k-dimensional representation that preserves a large fraction of the total variance. The proportion of variance captured by this truncated representation is

$$\mathrm{EVR}(k) = \frac{\sum_{i=1}^{k} \lambda_i}{\sum_{i=1}^{d} \lambda_i}.$$

A key property of PCA is the orthogonality of its components, which ensures decorrelation of the transformed variables.

3.1.2 Application to Source Separation

PCA can separate sources effectively when: (i) the mixing is approximately orthogonal, (ii) the sources are Gaussian (since decorrelation implies independence in that case), or (iii) the goal is to filter out low-variance noise, as PCA concentrates the high-variance components that capture the main signal on the first few PCs, and discards the rest as noise.

However, PCA does not guarantee independence, and thus cannot separate sources that are uncorrelated but statistically dependent. It may also miss meaningful sources with low variance. Covariance based, PCA groups computes uncorrelated sources. This approach works well for linear mixtures, where sources are indeed independent in the linear sense. However, it fails to separate sources in non-linear mixtures, where dependencies are more complex.

3.2 Independent Component Analysis (ICA)

3.2.1 Methodology

Independent Component Analysis (ICA), introduced by Comon (1994) and popularized by Hyvärinen & Oja (1999), seeks to recover statistically independent sources from observed mixtures. A detailed description can be found in Basak et al. (2004). Unlike PCA, which only decorrelates the data, ICA maximizes independence, typically measured through non-Gaussianity.

Given observed signals $\mathbf{D} = \mathbf{AS}$, where $\mathbf{S}$ are the unknown sources and $\mathbf{A}$ the mixing matrix, ICA estimates an unmixing matrix $\mathbf{W}$ such that

$$\mathbf{Y} = \mathbf{WD} \approx \mathbf{S}.$$

FastICA – written FICA here below– is a widely used algorithm for ICA, which proceeds by:

(i) Centering and whitening the data so its covariance becomes the identity.

(ii) Iteratively estimating independent components by maximizing a measure of non-Gaussianity, based on an estimation of the deviation from Gaussianity robust to outliers.

3.2.2 Application to Source Separation

ICA is powerful when sources are statistically independent and non-Gaussian. It has been widely applied in signal processing (e.g., EEG, speech separation). However, ICA cannot separate Gaussian sources, and is more computationally demanding than PCA.

3.3 Isometric Feature Mapping (Isomap)

3.3.1 Methodology

Isometric Feature Mapping (Isomap), introduced by Tenenbaum et al. (2000) and applied in an hydrology context in Jha et al. (2014), is a nonlinear dimensionality reduction method that extends classical Multidimensional Scaling (MDS, Borg & Groenen (2005)). Its goal is to preserve the intrinsic geometry of data lying on a low-dimensional manifold embedded in a high-dimensional space, i.e. to organize the data set in a simple, lower-dimensional structure while keeping the true shape and relationships of the data.

The method proceeds in three steps:

(i) **Neighborhood graph construction:** Build a graph where nodes are data points and edges connect nearest neighbors (typically k-nearest neighbors – 20 in our case – or within a fixed radius ϵ).

(ii) **Geodesic distance estimation:** Approximate geodesic distances between all pairs of points by computing shortest paths in the graph (in the `scikit-learn` implementation, by the Floyd-Warshall algorithm)

(iii) **Low-dimensional embedding:** Apply classical MDS to the matrix of estimated geodesic distances, yielding a k-dimensional embedding that preserves manifold structure.

3.3.2 Application to Source Separation

Isomap is capable of uncovering nonlinear mixing structures that linear methods such as PCA or ICA cannot capture. It has been used, for instance, to separate nonlinear mixtures of audio or image sources. However, it is computationally expensive for large datasets, sensitive to noise and outliers, and its performance depends critically on the choice of neighborhood size k.

3.4 Varimax-Rotated PCA

3.4.1 Methodology

Varimax rotation, introduced by Kaiser (1958) – see Richman (1986) for more details, is a classical post-processing step that can be applied to Principal Component Analysis (PCA). It aims to simplify interpretation by rotating the axes defined by the first k principal components, making the structure of the data more apparent. Specifically, varimax finds an orthogonal rotation that maximizes the variance of squared loadings for each component, so that each component is associated as clearly as possible with a subset of variables, without affecting the total explained variance.

Mathematically, let $\mathbf{V}_k$ be the matrix whose columns are the first k eigenvectors of the sample covariance matrix of $\mathbf{D}$, and let $\mathbf{\Lambda}_k$ be the diagonal matrix of the corresponding k largest eigenvalues. The (unnormalized) loadings matrix is then defined as

$$\mathbf{L}_k = \mathbf{V}_k \mathbf{\Lambda}_k^{1/2}$$

Varimax seeks an orthogonal rotation matrix $\mathbf{R}$ such that the rotated loadings

$$\mathbf{L}_k^* = \mathbf{L}_k \mathbf{R}$$

maximize the varimax criterion:

$$\mathrm{Varimax}(\mathbf{L}_k^*) = \sum_{j=1}^{k} \left[\frac{1}{d} \sum_{i=1}^{d} (l_{ij}^*)^4 - \left(\frac{1}{d} \sum_{i=1}^{d} (l_{ij}^*)^2 \right)^2 \right] \tag{2}$$

where l_{ij}^* are elements of the rotated loadings matrix $\mathbf{L}_k^*$, and d is the number of variables of the original data set. The orthogonality of $\mathbf{R}$ ensures that the rotated components remain uncorrelated.

The rotated principal components are then obtained as

$$\mathbf{Y}^* = \mathbf{D}\mathbf{V}_k\mathbf{R} = \mathbf{D}\mathbf{V}_k^*$$

3.4.2 Application to Source Separation

Varimax-rotated PCA is particularly useful when the underlying sources are expected to correspond to interpretable groups of variables. By redistributing variance across components, varimax can highlight latent factors that may not be evident in the unrotated solution. However, because varimax is based on second-order statistics (covariances), it does not guarantee statistical independence of the components, and its effectiveness depends on how well the rotated axes align with the true underlying structure (Abdi, 2003; Kaiser, 1958)

3.5 Factor Analysis (FA)

3.5.1 Methodology

Factor Analysis (FA), originally developed by Spearman (1904) and applied to geophysical data by Reed & Levin (1981), is a statistical method designed to explain the correlations among a set of observed variables in terms of a smaller number of unobserved latent variables, called *factors*. Unlike

PCA, which is purely algebraic and variance-maximizing, FA is based on a statistical model that explicitly accounts for measurement error.

Formally, FA assumes that each observation $\mathbf{d} \in \mathbb{R}^p$ can be written as

$$\mathbf{d} = \mathbf{\Lambda}\,\mathbf{f} + \boldsymbol{\epsilon}, \tag{3}$$

where $\mathbf{f} \in \mathbb{R}^k$ is a vector of latent factors, $\mathbf{\Lambda} \in \mathbb{R}^{p\times k}$ is the loading matrix, and $\boldsymbol{\epsilon} \in \mathbb{R}^p$ is a vector of unique errors. The factor loadings $\mathbf{\Lambda}$ describe the linear relationships between the observed variables and the latent factors. The unique errors $\boldsymbol{\epsilon}$ represent the part of the variance in each observed variable that is not explained by the common factors and are assumed to satisfy $\mathbb{E}[\boldsymbol{\epsilon}] = \mathbf{0}$ and $\mathrm{Cov}(\boldsymbol{\epsilon}) = \mathbf{\Psi}$, where $\mathbf{\Psi}$ is diagonal.

A standard identification assumption in FA is that the latent factors have zero mean and identity covariance, $\mathbb{E}[\mathbf{f}] = \mathbf{0}$ and $\mathrm{Cov}(\mathbf{f}) = \mathbf{I}_k$, and that $\mathbf{f}$ and $\boldsymbol{\epsilon}$ are uncorrelated. Under these assumptions, the covariance matrix of $\mathbf{d}$ implied by the factor model is

$$\tilde{\mathbf{\Sigma}} = \mathrm{Cov}(\mathbf{d}) = \mathbf{\Lambda}\,\mathbf{\Lambda}^T + \mathbf{\Psi}, \tag{4}$$

with $\mathbf{\Psi}$ diagonal. In what follows, we assume a multivariate normal distribution for the observations, $\mathbf{d} \sim \mathcal{N}(\mathbf{0}, \tilde{\mathbf{\Sigma}})$.

Let $\mathbf{D} \in \mathbb{R}^{n\times p}$ denote the data matrix, whose n rows are centered observations. The sample covariance matrix is defined as

$$\mathbf{\Sigma} = \frac{1}{n-1}\,\mathbf{D}^T\mathbf{D}. \tag{5}$$

Under the multivariate normal model, the log-likelihood (up to an additive constant) of the parameters $(\mathbf{\Lambda}, \mathbf{\Psi})$ can be written as (Lawley & Maxwell, 1971)

$$\log p(\mathbf{D} \mid \mathbf{\Lambda}, \mathbf{\Psi}) = -\frac{n}{2}\log|\tilde{\mathbf{\Sigma}}| - \frac{n}{2}\,\mathrm{tr}\big(\mathbf{\Sigma}\,\tilde{\mathbf{\Sigma}}^{-1}\big), \qquad \text{with } \tilde{\mathbf{\Sigma}} = \mathbf{\Lambda}\,\mathbf{\Lambda}^T + \mathbf{\Psi}. \tag{6}$$

Maximum likelihood estimation (MLE) consists in choosing $\mathbf{\Lambda}$ and $\mathbf{\Psi}$ so that the model-implied covariance $\tilde{\mathbf{\Sigma}}$ fits the empirical covariance $\mathbf{\Sigma}$ as closely as possible in this likelihood sense.

In the `scikit-learn` implementation of FA (`sklearn.decomposition.FactorAnalysis`) used here, the parameters are estimated by an expectation–maximization (EM) algorithm. At each E-step, sufficient statistics for the latent factors $\mathbf{f}$ are computed given the current estimates of $\mathbf{\Lambda}$ and $\mathbf{\Psi}$; at each M-step, $\mathbf{\Lambda}$ and $\mathbf{\Psi}$ are updated to maximize the expected log-likelihood.

3.5.2 Application to Source Separation

FA explicitly accounts for measurement error and reveals latent structures,which makes it valuable in exploratory analysis and as a probabilistic extension of PCA, especially when measurement errors cannot be ignored. However, assumptions such as linearity and uncorrelated errors may not hold in practice. In addition, factors are not guaranteed to be statistically independent, unlike ICA.

3.6 Empirical Orthogonal Teleconnection (EOT) Analysis

3.6.1 Methodology

Empirical Orthogonal Teleconnection (EOT) analysis, introduced by Van Den Dool et al. (2000), is an extension of PCA. While PCs maximize captured variance, EOT seeks to identify spatially coherent *teleconnection patterns*, anchored at specific base points.

The procedure can be summarized as follows:

(i) Select a candidate base point with time series $\mathbf{x}_b$.

(ii) Regress $\mathbf{x}_b$ against all spatial time series in the dataset to obtain a regression pattern $\mathbf{p}_b$:

$$\mathbf{p}_b = \frac{\mathbf{D}^T \mathbf{x}_b}{\|\mathbf{x}_b\|^2}.$$

(iii) Evaluate the residual variance after removing the contribution of $\mathbf{p}_b$.

(iv) Choose the base point that minimizes this residual variance as the first EOT.

(v) Repeat iteratively on the residuals until a stopping criterion is reached (in our case, a fixed number of patterns).

Unlike PCs, which produce orthogonal modes, EOT components are constructed to maximize captured variance associated with localized time series, leading to patterns that are often easier to interpret physically.

3.6.2 Application to Source Separation

EOT is particularly suited to geosciences, where the sources of variability often correspond to large-scale climatic modes (e.g., ENSO, NAO). By anchoring patterns to specific time series, EOT produces spatial structures that can be directly related to physical drivers. However, its reliance on linear regression and orthogonalization can distort the physical meaning of higher-order modes, and the method may overlook weaker sources not well represented by base points.

3.7 Non-Negative Matrix Factorization (NMF)

3.7.1 Methodology

Non-Negative Matrix Factorization (NMF), introduced by Lee & Seung (1999)and applied to sediment reflectance spectrum unmixing in Lee et al. (2007), is a parts-based decomposition method for non-negative data. Given a non-negative matrix $\mathbf{D} \in \mathbb{R}_{\geq 0}^{n \times d}$, NMF seeks two non-negative matrices $\mathbf{W} \in \mathbb{R}_{\geq 0}^{n \times k}$ and $\mathbf{H} \in \mathbb{R}_{\geq 0}^{k \times d}$ such that

$$\mathbf{D} \approx \mathbf{W}\mathbf{H}.$$

where the columns of $\mathbf{W}$ represent basis vectors (or components) and the rows of $\mathbf{H}$ are the weights (or activations) of each basis vector across the variables.

The factorization is usually obtained by minimizing a reconstruction error, e.g. the Frobenius norm,often solved by multiplicative update rules or alternating least squares:

$$\min_{\mathbf{W},\mathbf{H} \geq 0} \|\mathbf{D} - \mathbf{W}\mathbf{H}\|_F^2,$$

.

The Frobenius norm is defined as

$$\|\mathbf{D} - \mathbf{W}\mathbf{H}\|_F = \sqrt{\sum_{i,j} (\mathbf{D}_{i,j} - (\mathbf{W}\mathbf{H})_{i,j})^2}$$

The optimization problem is solved using the following iterative algorithm:

$$\mathbf{H} \leftarrow \mathbf{H} \odot \frac{\mathbf{W}^T\mathbf{D}}{\mathbf{W}^T\mathbf{W}\mathbf{H}},$$

$$\mathbf{W} \leftarrow \mathbf{W} \odot \frac{\mathbf{D}\mathbf{H}^T}{\mathbf{W}\mathbf{H}\mathbf{H}^T},$$

where $\odot$ denotes element-wise multiplication.

3.7.2 Application to Source Separation

The non-negativity constraint enforces additivity, yielding sparse and interpretable factors. NMF has proven effective in applications where signals are naturally non-negative (e.g., spectral unmixing, document classification, image processing). Its ability to extract additive, localized features makes it attractive for source separation. However, NMF solutions are not unique, depend strongly on initialization, and require the number of components k to be pre-specified.

4 SIMULATION SETUP

The purpose of the simulations is not to reproduce the full complexity of endogenous or climate processes, but to provide a controlled and flexible framework in which the performance of BSS methods can be rigorously assessed. To this end, we construct synthetic geodetic datasets that mimic the main ingredients of real observations: (i) endogenous signals with simple yet representative temporal behaviors, (ii) climate signals with realistic spectral properties and non-stationarity, and (iii) stochastic noise combining white and power-law components.

From a statistical time-series perspective, the usual noise/signal contrast is between stationary and transient behavior. Here, however, we focus on a multivariate notion of coherence: patterns that are shared across several series are referred to as *signal*, while patterns that differ from one series to another are referred to as *noise*.

This framework allows us to systematically vary key factors such as the number of stations, the number and type of sources, the amplitude of noise, and the relative strength of endogenous versus climate contributions. By exploring a broad set of controlled scenarios, we can isolate the conditions under which BSS methods succeed or fail, and thereby obtain general insights that would be difficult to extract directly from real data.

4.1 Principle of the simulations

To evaluate the performance of BSS methods in a controlled environment, we simulate synthetic monthly geodetic datasets that span 20 years. Each dataset consists of L geodetic time series ($8 \leq L \leq 20$), in which endogenous and climatic sources are combined with stochastic noise. The observed signal at station ℓ and time t is written, as stated in Eq. (1), as

$$D_\ell(t) \;=\; \sum_{j=1}^{J} g_{\ell j}\, G_j(t) \;+\; \sum_{k=1}^{K} c_{\ell k}\, C_k(t) \;+\; N_\ell(t),$$

where $G_j(t)$ are the endogenous sources, $C_k(t)$ the climatic sources, and $N_\ell(t)$ the noise. The coefficients $g_{\ell j}$ and $c_{\ell k}$ encode the spatial mixing of the sources. By construction, all sources are independent processes and the noise is not correlated with both endogenous and climatic signals. This idealized framework is not meant to reproduce the full complexity of real Earth processes, nor realistic geographical patterns, but to provide a rigorous testbed for BSS methods under controlled conditions. Indeed, the methods considered (PCA, ICA, Varimax, etc.) rely only on the statistical properties of the signals — temporal correlations, (in)dependence, and spectral content — rather than on their geographical structure. Accordingly, we use a limited number of synthetic time series with realistic temporal variability and frequency content, reflecting the strong redundancy introduced by large-scale geophysical structures, which makes the effective number of independent series much smaller than the number of stations. Our experiments confirm that increasing the number of series has only a limited impact on the results (see Section 5.3), so imposing explicit geographical patterns would mainly increase computational cost without changing the evaluation of BSS methods. This controlled environment allows us to quantify performance across a wide range of scenarios and to identify the conditions under which BSS methods can, or cannot, recover meaningful endogenous signals.

The spatial structure of the synthetic sources is controlled by the mixing matrix. Each source has mixing coefficients assigned across the network, drawn randomly, so that individual sources contribute with varying amplitude to different time series. As a consequence, the ensemble of simulated configurations spans a continuum of effective spatial extents, from sources contributing comparably to most of the network to sources whose contribution is concentrated on a small subset of stations. From the standpoint of BSS, the spatial extent of a source and its amplitude are not independent controls: what governs separability is the fraction of the total variance carried by the source, which is jointly determined by its amplitude (parameterised here by the endogenous-to-climate ratio R) and by the number of time series over which it is expressed. Varying the network size L at fixed R therefore probes, in effect, the role of the spatial footprint of the signal of interest relative to the analysed network.

4.2 Definition of the sources

4.2.1 Endogenous signals

Endogenous sources are modeled using six simple parametric functions that represent typical temporal behaviors observed in deep interior processes of the Earth (Ballu et al., 2019; Bevis & Brown, 2014).

- a Heaviside function,
- a linear slope (possibly delayed),
- a logarithmic transient,
- a sinusoid with random frequency and phase,
- an exponential decay (relaxation),
- a gate function, mimicking time-limited events.

For each simulation, the parameters (onset times, amplitudes, slopes, frequencies, etc.) are drawn independently from uniform distributions, ensuring variability across realizations.

4.2.2 Climatic signals

The climatic contribution is simulated from standardized indices representing large-scale modes of climate variability: Southern Oscillation Index (SOI), Arctic Oscillation (AO), North Atlantic Oscillation (NAO), Pacific Decadal Oscillation (PDO), Atlantic Multidecadal Oscillation (AMO), and Atlantic Meridional Mode (AMM). For each simulation, one or two indices are randomly selected and normalized to zero mean and unit variance. These signals introduce realistic non-stationary variability with broad spectral content. The time series of the climate indices are provided by the NOAA Physical Sciences Laboratory (2009) on their webpage `https://psl.noaa.gov/data/climateindices/list/`.

Although the target endogenous signals are intentionally simple, the climate sources — modeled using autoregressive processes or normalized climate indices — introduce stochastic variability and departures from strict stationarity (i.e., some statistical properties change over time), making the source separation problem intrinsically nontrivial.

4.2.3 Noise

The noise $N_\ell(t)$ combines independent realizations of white and power-law noise at each station, both with variance σ^2. Power-law noise has a power spectral density

$$P(f) \propto f^\kappa, \tag{7}$$

with κ, the spectral index, randomly drawn from a uniform distribution in $[-2, 1]$ (Agnew, 1992; Gobron et al., 2021), covering the typical range of GNSS noise processes. White noise corresponds to the special case $\kappa = 0$. Noise series are generated using the algorithm of Timmer & Koenig (1995), as implemented in the `colorednoise` package (Patzelt, 2023).

4.3 Organization of the simulations

We evaluate each BSS method on 1,000 independent simulations for each of 120 configurations, obtained by combining the parameters listed in Table 1. The experimental design systematically explores:

- the number of stations $L \in 8, 12, 16, 20$,
- the number of endogenous ($J = 1, 2$) and climate ($K = 0, 1, 2$) sources,
- the noise amplitude $\sigma \in 0.1, 0.25, 0.5, 0.75, 1$,
- the endogenous-to-climate signal ratio R, with 13 values ranging from 0.01 to 2.0.

All possible combinations are generated exhaustively, without subsampling, to ensure exhaustive coverage of the parameter space. Within each configuration, randomness is introduced through independent realizations of the stochastic noise, the selection of climate indices, and the selection and parameters of the endogenous functions.

For clarity, Equation (1) can be rewritten in the explicit simulation form:

$$D_\ell(t_i) = R \sum_{j=1}^{J} g_{\ell j} G_j(t_i) + \sum_{k=1}^{K} c_{\ell k} C_k(t_i) + \sigma N^\ell_{\text{PowerLaw}}(t_i) + \sigma N^\ell_{\text{White}}(t_i) \tag{8}$$

where the amplitudes $g_{\ell j}$ and $c_{\ell k}$ are independently drawn from uniform distributions $\mathcal{U}[0, 1]$, ensuring station-to-station variability.

An example of simulated data is provided in Figure 1, a pseudo-code algorithm for simulation is provided in Appendix A.

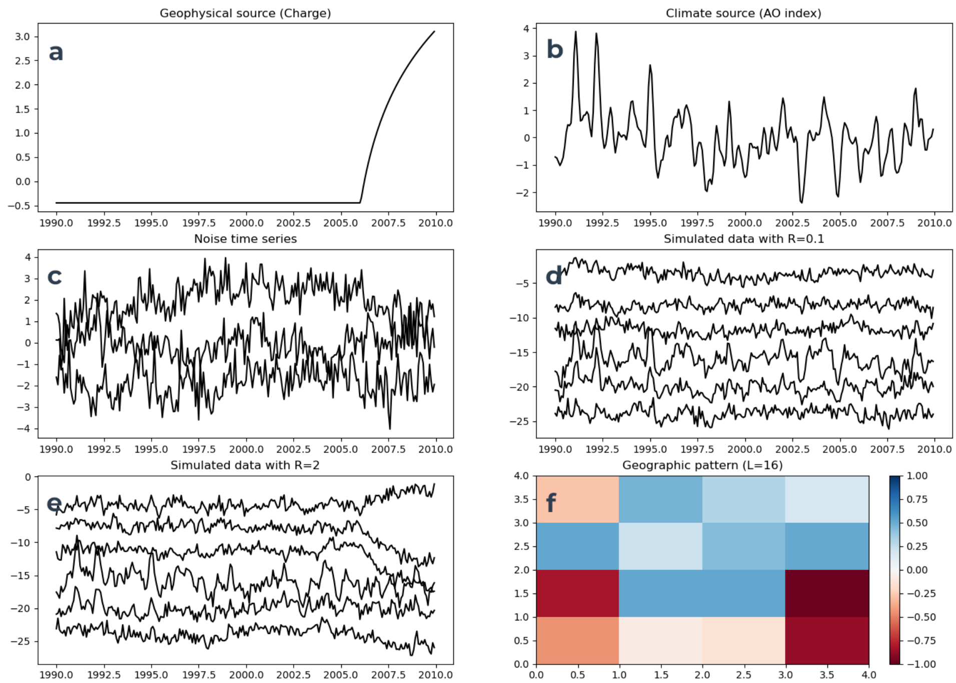

Figure 1. Example of a single realisation of the synthetic generator. (a) A endogenous source time series (charge starting end of 2005). (b) A climate-related source, the AO index. (c) Incoherent noise realisation for three arbitrary stations (arbitrary shift for readability). (d) Resulting mixed time series for six stations of the network, for a low endogenous-to-climate ratio ($R = 0.1$) (arbitrary shift for readability), and (e) for a high ratio ($R = 2$). (f) Spatial distribution of the mixing coefficients of the endogenous source over the 16-stations network. Units are arbitrary. This figure illustrates a single configuration among the 120 tested; a full generator is available in the accompanying repository.

4.4 Evaluation of the methods

Each BSS method is applied both to the simulated data (8) and to a null data set where the endogenous signal is set to zero, providing a baseline for comparison. For every simulation, the five modes that capture the largest variance are retained. The endogenous source is identified as the mode that maximizes the correlation with the true source. Performance is quantified by the correlation between the retrieved endogenous signals and the simulated space-time endogenous signals. Temporal and spatial correlations were also evaluated separately but showed similar results and are not discussed further.

L	Number of stations	8, 12, 16, 20
J	Number of endogenous sources	1, 2
K	Number of climate sources	0, 1, 2
$C_k(t)$	Climate indices	SOI, AO, NAO, PDO, AMO, AMM
$G_j(t)$	Endogenous signals	Heaviside, slope, delayed slope, log. transient, sinusoid, exponential decay, gate
$N^{\ell}_{\mathrm{PowerLaw}}(t)$	Local power-law noise	indep. per station, $\kappa \in [-2, 1]$
$N^{\ell}_{\mathrm{White}}(t)$	Local white noise	indep. per station
σ	Noise amplitude	0.1, 0.25, 0.5, 0.75, 1
R	Endogenous/climate ratio	0.01–2.0 (13 values)
$g_{\ell j}, c_{\ell k}$	Mixing coefficients	$\mathcal{U}[0, 1]$

Table 1. Parameter space explored in the simulations.

5 RESULTS FOR THE SYNTHETIC CASE

5.1 Performance for detection and separation

Figure 2 summarizes the empirical distributions of correlations between the retrieved endogenous signals and the true (simulated) space-time endogenous signals, across thousands of synthetic realizations. For each method and for different values of the internal/external ratio (R), we report the 2.5%, 25%, 50% (median), 75%, and 97.5% percentiles. This representation illustrates not only the central tendency of the results but also their variability. The spread of these distributions provides a direct measure of uncertainty, showing in which conditions the methods perform consistently and in which cases they yield more variable outcomes.

Building on these results, Figure 3 and 4 show the proportions of the simulations that exceed specified thresholds. The detection threshold is calibrated empirically on a zero-source baseline. For each simulation, a companion dataset is generated in which the endogenous source is omitted while the climate sources, the spatial patterns and the noise realisation are left unchanged. The same decomposition is applied to this baseline, the same maximum over the five leading modes is retained, and the 95th percentile of the resulting distribution of correlations defines the threshold above which a detection is declared. Selecting the maximum over five modes inflates the resulting correlation relative to what a single mode would yield, since the best of several candidates is retained rather than a single realization. However, this inflation is common to both the signal-present and signal-absent cases, as the same selection rule is applied to each. It therefore affects both distributions in the same way and does not bias their comparison. The threshold therefore quantifies what the procedure returns when no endogenous source is present, rather than what would be expected from a single uncorrelated pair of

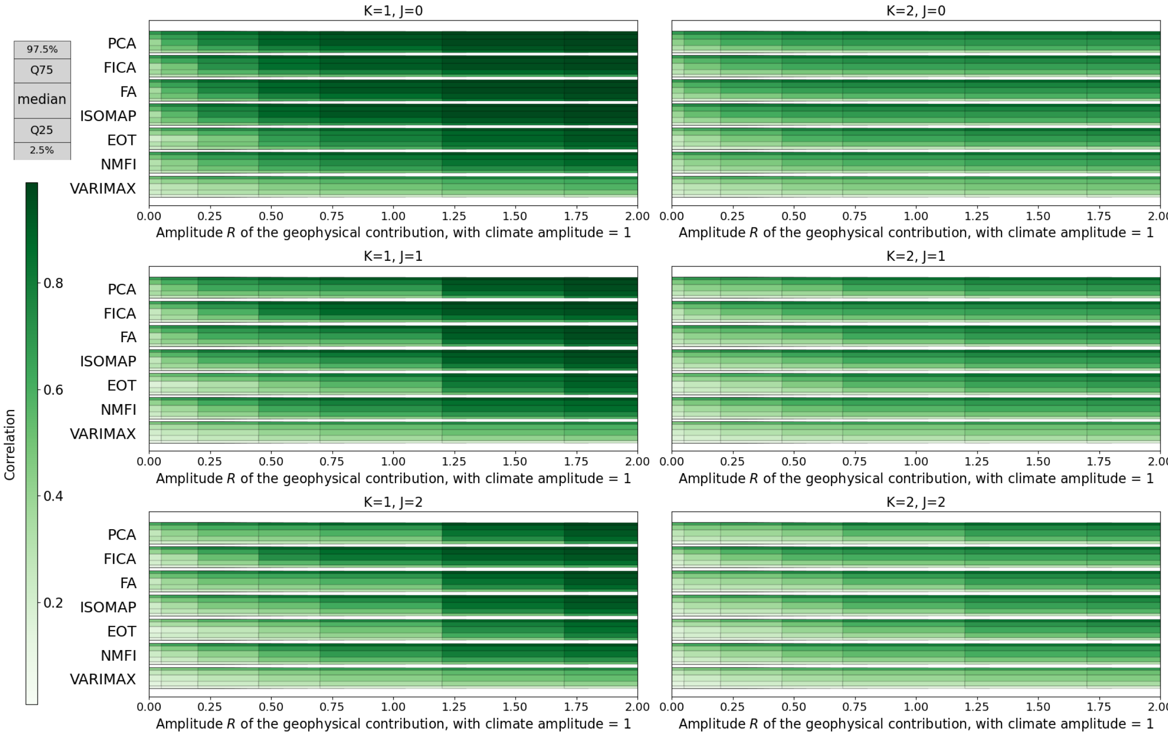

Figure 2. Performance of the different source separation methods as a function of the internal/external ratio (R). For each method, the shaded bands represent the empirical distribution of correlation values between the retrieved endogenous signals and the real space-time endogenous signals across simulations (2.5%, 25%, 50%, 75%, and 97.5% percentiles), as a function of the amplitude R of the endogenous contribution. This quantifies the uncertainty of the separation performance under varying conditions. K and J are the number of climatic and endogenous sources, respectively.

time series. It corresponds to a detection at the 95%-significance level. This stringent criterion ensures that detected signals are statistically significant and not due to chance.

Using this definition, we ranked the space-time correlations between retrieved and original sources across all simulations. Figure 3 shows boundaries corresponding to the detection at a 95% significance level (black), and iso-correlation contours at 0.5 (red), 0.7 (orange), and 0.8 (green), plotted as functions of the endogenous-to-climate ratio. The results are categorized by the number of endogenous and climate sources present.

For example, a red line at 60% would indicate that 60% of the simulations yield correlations less than or equal to 0.5, whereas a green line at 90% would mean that only 10% of the simulations reach or exceed a correlation of 0.8.

We present results for the three best-performing methods: PCA (solid line), Isomap projection (dashed line), and FICA (dotted line). These are the only methods that ever ranked as the best in any tested scenario; all other methods consistently underperformed and were never competitive. The background color on each plot reflects the best performance achieved by any tested method under the corresponding conditions. For instance, the grey region visible in the lower-left part of each graph indicates that no method attained significant correlation in more than 25% of simulations for those configurations. Conversely, when the endogenous-to-climate ratio reaches 0.5, detection is possible in over 95% of simulations using either PCA or Isomap, even when two climate and two endogenous sources coexist, as highlighted by the red and black contours. Changes in the background color consistently coincide with one of the lines for PCA, FICA, or Isomap, further confirming that these three methods dominate the performance rankings.

Isomap occasionally matches PCA's performance but is never the sole best-performing method. PCA excels particularly when no climate sources are present or when the endogenous-to-climate ratio is either very low or very high. FICA surpasses PCA in intermediate ranges of this ratio.

An intriguing observation is that PCA's ability to separate the endogenous signal locally diminishes as the signal-to-noise ratio increases. The magenta line on the plots shows the fraction of simulations where PCA achieves a climate signal separation correlation of 0.7. When the endogenous signal is weak and only one climate source exists (middle column), PCA effectively isolates the climate signal. However, as the endogenous signal strengthens (for R between 0.5 and 1), separation quality decreases because the methods struggle to disentangle overlapping climate and endogenous contributions. When the endogenous signal eventually matches or exceeds the climate contribution, its separation quality improves, which in turn enhances climate signal retrieval.

Applied to the present results, the proposed detection criterion, based on comparison with no-endogenous-source simulations, shows that the tested BSS methods, particularly PCA, FICA, and ISOMAP, can identify weak endogenous signals even amid dominant climate variability, with the proportion of successful detections providing a quantitative measure of performance at a controlled false-alarm rate. However, this detection does not always guarantee a strong quantitative match between the extracted and true sources. In other words, although BSS methods can uncover weak and unexpected endogenous signals even in complex datasets, the strength of the correlation is sometimes too low to build sound physical interpretations. This highlights a dual aspect of their performance: statistical detection is not always synonymous with interpretability.

To address this, we define an additional reliability threshold: a correlation of 80%, which corresponds to capturing about two-thirds (64%) of the variance of the original endogenous source. Only when this level is exceeded can the retrieved signal be considered a reliable proxy of the true endogenous process. Below this threshold, interpretations should be made with caution.

Furthermore, the green regions on the graphs indicate that effective separation requires the amplitude of the endogenous signal to be at least comparable to that of climate variability. Otherwise, even

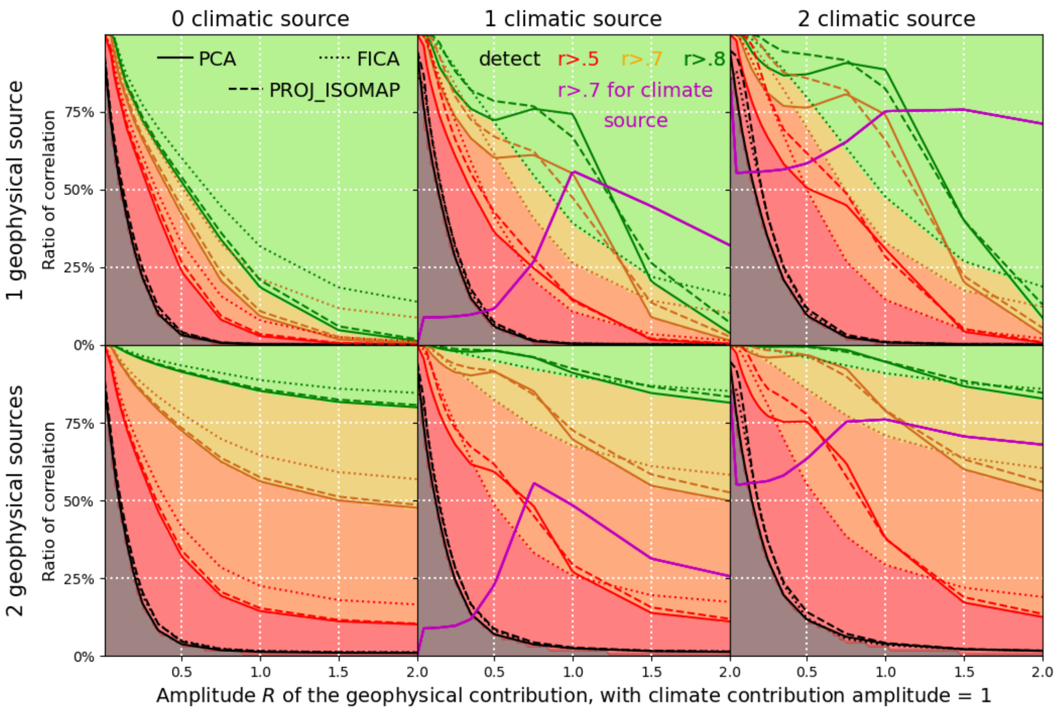

Figure 3. Proportion of simulations in which the correlation between the retrieved and original endogenous source exceeds specified thresholds, shown as a function of the numbers of endogenous and climate sources. Detection thresholds are represented in black and grey; correlations of 0.5, 0.7, and 0.8 are shown in red, orange, and green, respectively. The magenta line represents the 0.7 correlation threshold for the climate source. The three top-performing methods — PCA, FICA, and Isomap projection — are highlighted with solid, dotted, and dashed lines, respectively. The background color indicates, for each configuration, the highest correlation threshold reached by the best-performing method among the seven tested.

detectable signals may not be sufficiently extracted for meaningful analysis. This challenge becomes more pronounced when multiple internal sources coexist.

5.2 Impact of the type of endogenous source

To evaluate whether BSS method performance or optimality depends on the type of endogenous signal, Figure 4 presents the same statistics disaggregated by signal type. The results show that BSS methods perform consistently across different types of endogenous signals. However, for the relaxation process – and to a lesser extent the sine signal – FICA outperforms the other methods at intermediate endogenous-to-climate ratios. For other signal types, FICA and Isomap projection share the best performance at medium ratios, while PCA consistently excels at the lowest and highest ratios.

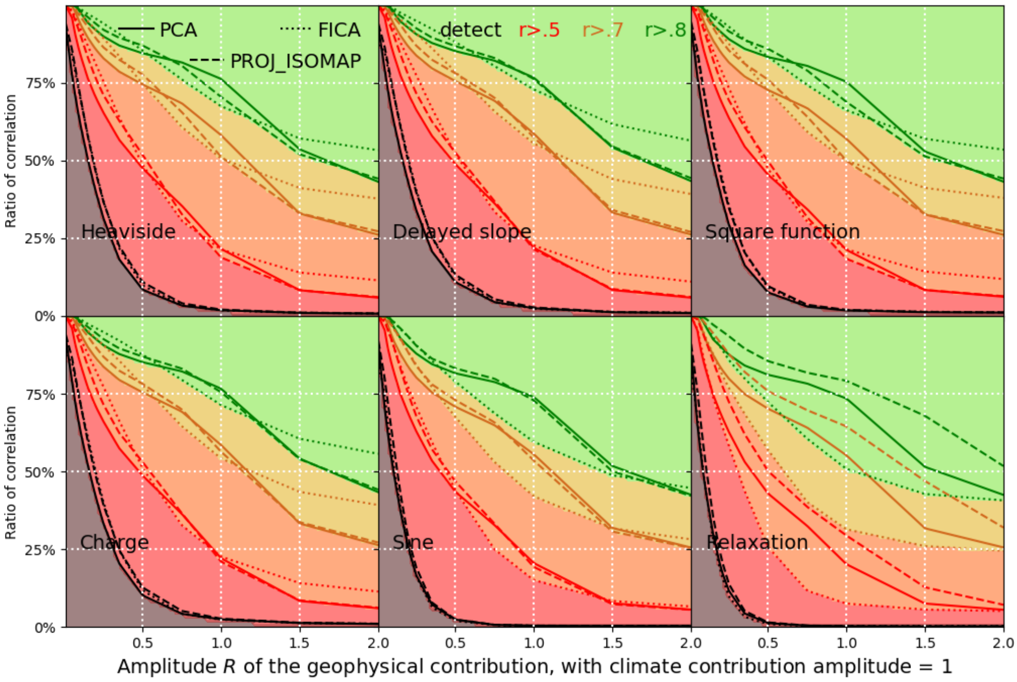

Figure 4. Proportion of simulations in which the correlation between the retrieved and original endogenous source exceeds specified thresholds, shown as a function of the endogenous source type. Detection thresholds are represented in black and grey; correlations of 0.5, 0.7, and 0.8 are shown in red, orange, and green, respectively. The three top-performing methods — PCA, FICA, and Isomap projection – are highlighted with solid, dotted, and dashed lines, respectively. The background color indicates, for each configuration, the highest correlation threshold reached by the best-performing method among the seven tested.

5.3 Impact of the number of time series and noise level

To assess the effect of the number of time series on source separation performance, we compared configurations differing only in this parameter. For each pair of values (L = 8 vs 12, 8 vs 16, 8 vs 20, 12 vs 16, 12 vs 20, and 16 vs 20), we computed the difference in mean correlation between the retrieved and true sources. We then fitted a least-squares regression model to these differences in order to estimate the relative contribution of each L value to overall performance. A constraint was applied to ensure that the sum of all contributions equals zero, allowing the resulting coefficients to be interpreted as deviations from the average correlation.

This analysis revealed a monotonic positive relationship between the number of time series and the quality of source separation. In particular, configurations with L = 20 showed an average correlation approximately 0.08 higher than those with L = 8. However, the magnitude of this improvement depended on the endogenous-to-climate signal ratio (R). It was minimal (about 0.02) when R was very low, peaked at 0.12 when $R \simeq$0.5, and declined again to 0.08 as R increased to 2. This pattern is consistent with the behaviour illustrated in Figure 3, where separation performance is reduced when endogenous and climate signals have comparable amplitudes – roughly in the range R = 0.5 to 1.5.

The influence of station number L also depends on the BSS method: least effective methods (e.g., EOT and Varimax) show minimal improvements (0.053 and 0.056), while PCA and FA benefit most (0.101 and 0.102). Intermediate gains are observed for Isomap projection (0.076), NMF (0.083), and FICA (0.087). Additionally, source type affects the impact magnitude, from 0.018 for delayed slope and charge, up to 0.29 for square functions.

Using the same approach, we analyzed the effect of incoherent noise level on correlation. We focus on the extreme cases $\sigma = 0.1$ and $\sigma = 1$, which reveal an average correlation decrease of 0.28 across all scenarios and BSS methods. The impact of noise varies as a function of R: it initially causes a modest correlation decrease of 0.02 at $R = 0.01$, a regime in which the correlation is nearly zero regardless of the noise. The effect reaches its maximum around $R = 0.25$, with a correlation decrease of 0.47, and then gradually diminishes, resulting in a decrease of only 0.08 when $R = 2$. This pattern mirrors that observed for station number: noise most strongly degrades correlation at intermediate signal-to-noise ratios, where source separation is possible but challenging.

Noise impact varies little between BSS methods, except Varimax, which shows a smaller decrease (0.15) due to its overall weaker performance. Similarly, the type of endogenous source generally has limited effect on noise sensitivity, except for relaxation (0.16 correlation decrease) and the square function (0.44 decrease).

5.4 Why some methods outperform others

The ranking observed reflects the match, or mismatch, between each method's assumptions and the structure of our generative model: a dense, linear, signed mixture of independent sources plus noise, $D = AS+N$, as expected for geodetic networks. Two factors govern performance: whether a method's structural constraints are compatible with such a mixture, and, among compatible methods, the statistical cost of its criterion, second-order moments, i.e. variance and covariance, being far more robustly estimated than higher-order or locally-defined statistics.

PCA is optimal in the least-squares sense for dense random mixing vectors, which are nearly orthogonal in high dimension, and relies only on second-order statistics with a single free parameter—hence its robustness at low SNR or short records. Its limitation is the rotational indeterminacy among comparable eigenvalues, which caps its performance once SNR improves.

ICA resolves this indeterminacy using non-Gaussianity, matching the maximum-likelihood estimator for our strongly non-Gaussian sources, but at the cost of less robust fourth-order statistics, explaining why it overtakes PCA when the signal is well-expressed but degrades faster under noise. This also explains the apparent reversal at high internal/climate ratios: when endogenous sources dominate, the eigenvalue spectrum becomes hierarchical and PCA alone identifies the individual sources; ICA's whitening step then discards this useful hierarchy and amplifies noise in poorly-constrained directions, adding estimation cost without identification gain.

Isomap, though nonlinear, degenerates to a PCA-like solution here because the manifold is in fact an affine subspace, so its success reflects graceful degeneracy rather than genuine nonlinear structure—unlike other nonlinear methods, whose extra parameters only add variance.

Factor analysis shares PCA's rotational indeterminacy but must additionally absorb spatially coherent non-endogenous variability into its factors, incurring cost without benefit.

The remaining three methods fail because they impose structure the mixture lacks: Varimax seeks sparse loadings, incompatible with dense mixing vectors; EOT assumes near-pure sources exist at some station, which they do not; NMF requires non-negativity (forcing a spurious near-constant shift component) and a separability assumption likewise violated here. Unlike the noise-driven errors above, these are specification biases that persist regardless of SNR or record length.

None of this is a criticism of these methods generally, they suit settings where their assumptions hold (e.g., EOT and NMF for hyperspectral unmixing with pure endmembers). Rather, the dense, signed, approximately linear character of geodetic mixtures simply selects for a specific subset of methods.

5.5 Conclusions from the synthetic tests

To assess theefficiency of Blind Source Separation (BSS) methods in separating weak endogenous signals from dominant climate variability, we conducted synthetic tests with controlled amplitude ratios between the two signals. For each test, we applied 7 BSS methods, each producing 5 modes (or components). The endogenous signal was considered successfully detected if the highest correlation between any of the 5 retrieved modes and the original endogenous signal exceeded the 95th percentile of the highest correlations obtained from simulations where no endogenous signal was included. This threshold ensures statistical significance in detection, accounting for the best possible match among all modes and methods. Our results demonstrate that BSS methods, particularly PCA, FICA, and Isomap projection, can effectively detect the endogenous signal even when its amplitude is noticeably smaller than that of the climate signal. Detection performance scales with the relative strength of the endogenous signal, as illustrated by the following retrieval rates:

For a endogenous-to-climate amplitude ratio of 1:20, the retrieval rate was 25%. For a ratio of

1:6.7 (15%), the retrieval rate increased to 50%. For ratio of 1:3–4 (25–33%), the retrieval rate reached 75%. Thus, BSS methods can detect endogenous signals despite climate signals being 6 to 20 times larger in amplitude, with the detection based on the best-performing mode among the 5 modes for each method, and the best-performing method among the 7 tested.

However, when R is below one, over 40% of simulations show correlations between the retrieved and true sources below 0.8, even in the most favorable scenario of a single climate source mixed with a endogenous source. This corresponds to capturing less than two-thirds of the true signal variance, a level of accuracy insufficient for sound physical characterization of the endogenous process.

These results caution against using BSS methods for a detailed characterization of endogenous sources due to their limited ability to accurately recover source structures. Instead, BSS should primarily be employed for detecting unexpected signals, which can then be analyzed in depth with less blind, more targeted methods to better resolve their space-time characteristics.

6 COMPARISON WITH A DEEP-LEARNING ALGORITHM

Recent studies have explored machine learning as an alternative approach to separating endogenous signals of different origins, testing a variety of architectures and learning strategies on observational datasets (Murtagh, 1991; Kiani Shahvandi et al., 2024a,b), thereby complementing BSS techniques and enriching the range of tools available for signal separation in geosciences.

To compare with the BSS analysis, we implemented a neural network designed to learn source separation directly from the data. More precisely, we chose an autoencoder architecture with a dual decoder. This is a highly effective structure for source separation or matrix factorization, as it enforces a common latent representation before reconstructing two distinct components. The model takes the observed time series (a matrix of L series of length N) and passes them through an *encoder* that embeds the information into a compact latent representation. The encoder aims to represent the data efficiently by removing redundancy and/or discarding less important information. From this embedding, two *decoders* simultaneously reconstruct (i) the source signals S that can be interpreted as the arrangement of K distinct source vectors and (ii) the mixing coefficients A. Training is performed on 10,000 synthetic mixtures where the true sources are known, allowing the network to learn how to separate them. Once trained, the model is evaluated on new test sets. The network architecture is shown in Fig. 5.The diagram illustrates the complete data flow, from input $\mathbf{D} \in \mathbb{R}^{L\times N}$ to the two predicted outputs A_{pred} and S_{pred}.

To avoid overfitting, the training set was enriched with a broad family of synthetic endogenous signals (e.g., sawtooth, noisy square waves, random walks with trend) and with climate surrogates generated by phase randomization (Theiler et al., 1992). Without such diversification, the network

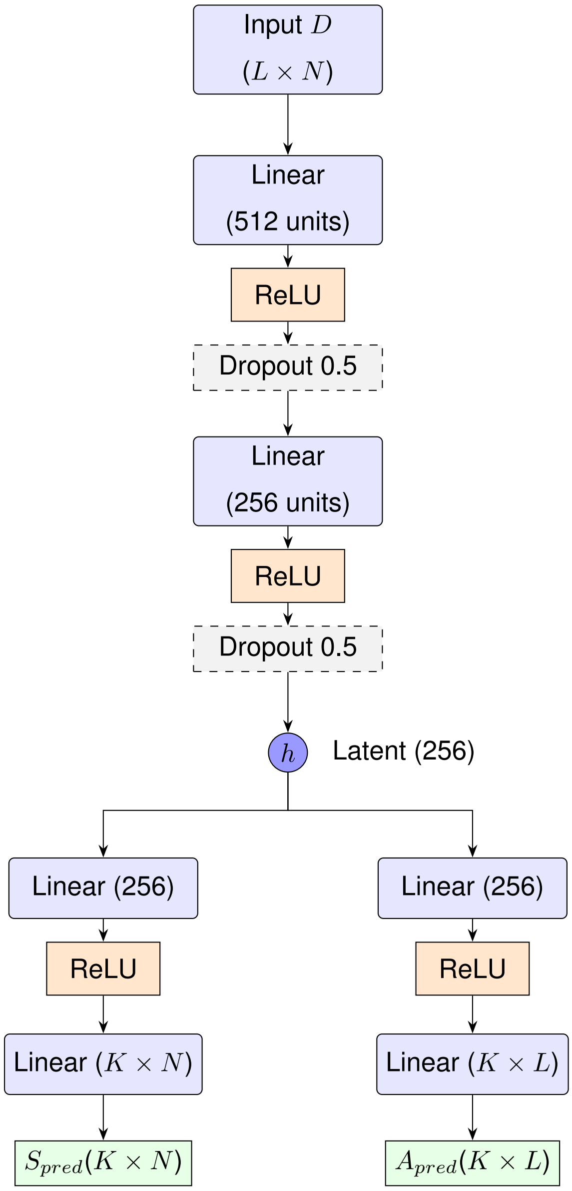

Figure 5. Neural network architecture used for signal separation. The encoder compresses the input data into a latent representation (embedding), from which two decoders reconstruct the source signals S and the mixing coefficients A.

simply memorizes the training signals and fails on unseen data. Training optimizes the network using the correlation between reconstructed and true observations ($A_{\mathrm{pred}}S_{\mathrm{pred}}$ vs. AS), with performance saturating after approximately 1,000 iterations. Moreover, dropout layers were inserted into the network as a regularization mechanism: at each training step, a random subset of units is temporarily deactivated, which discourages complex co-adaptations and has been shown to reduce overfitting in deep neural networks (Srivastava et al., 2014).

We then compared the neural network with PCA and ICA, the best-performing BSS methods. All

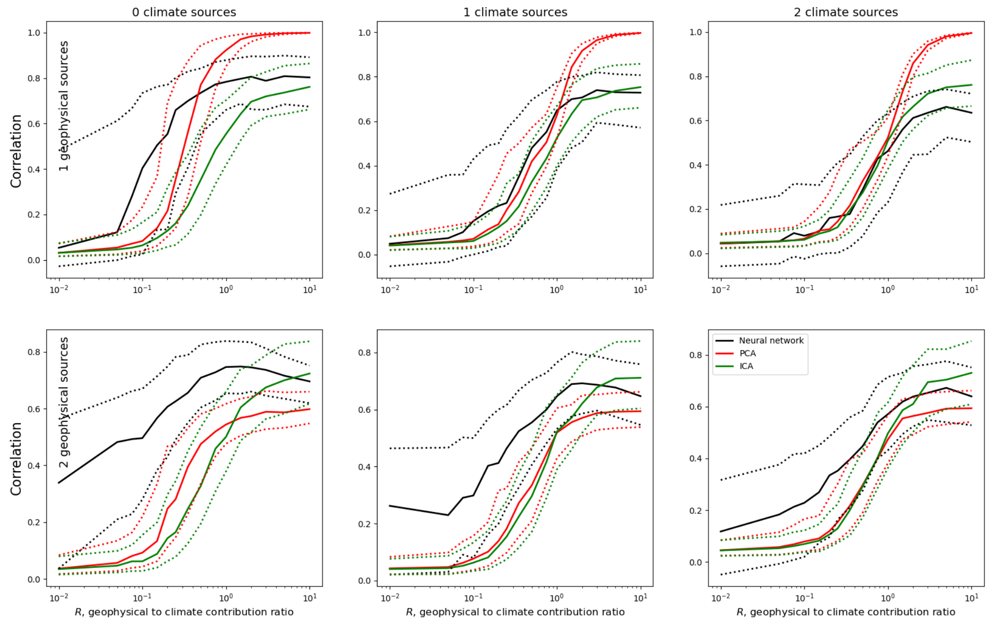

Figure 6. Comparison between the performance of a neural network (black), PCA (red) and ICA (green) as a function of the R ratio between endogenous and climate sources. The median correlation (between the space-time signature of the retrieved source and that of the input sources) is shown as a solid line, whereas the 25th and 75th percentile lines are shown with dashed line.

methods were evaluated on 10,000 independent test sets for fixed numbers of endogenous ($J = 1, 2$) and climate ($K = 0, 1, 2$) sources, using the correlation between retrieved and true spatio-temporal patterns as the metric (Fig. 6). Results are sorted by the endogenous-to-climate contribution ratio R.

The comparison shows that the neural network can match or exceed BSS methods when the endogenous signal is weak (low R). However, correlations remain too low for physical interpretation, with a maximum median of 0.81 (just reaching our 0.8 criterion), whereas PCA achieves values above 0.95 in the same configuration. When the number of endogenous sources increases, the neural network fails to recover them reliably, while PCA and ICA, although degraded, remain competitive. The percentile envelopes also show that neural network predictions are less stable across realizations than PCA, especially when multiple sources coexist.

Overall, this experiment suggests that a simple neural network can rival BSS methods only in very noisy conditions, and even then does not provide reconstructions accurate enough for geophysical interpretation. This comparison is somewhat unfair to BSS methods: unlike neural networks, BSS methods do not require training, do not depend on fixed numbers of time series or sources, and can reveal unexpected signals. While more sophisticated architectures might alleviate some of these limitations,

Table 2. Comparison between BSS methods and recent machine learning (ML/DL) approaches for signal separation.

	BSS methods (e.g. PCA, ICA)	**ML/DL methods (e.g. physics-informed NN, autoencoders)**
Prior knowledge	Minimal (blind separation; only statistical assumptions such as independence or orthogonality)	Require training data, labels, or strong priors (e.g. physics constraints, known wave modes)
Data requirement	Directly applicable to raw observations, no training set needed	Training phase often requires large synthetic or observed datasets
Interpretability	Clear statistical interpretation (e.g. variance explained, independence of components)	Often a black box; interpretation depends on architecture and training
Reliability	Performance limited when signals overlap strongly or SNR is low	Can capture nonlinearities and complex structures if trained adequately
Applicability	Suitable when little is known about the sources (e.g. poorly characterized interior signals)	Powerful when prior models exist, but less transferable if source properties are uncertain
Examples in geosciences	Extraction of climate and endogenous modes in geodetic data (e.g. NAO, GIA, earthquakes)	Physics-informed models for polar motion, seismic mode separation, or guided autoencoders

our test highlights that in the present context BSS remains competitive with respect to neural networks. Table 2 summarizes the main conceptual differences between BSS methods and recent deep-learning approaches. While machine learning models can capture nonlinearities and complex structures when sufficient prior knowledge and training data are available, they are not blind in the strict sense. In contrast, BSS methods operate with minimal assumptions and can be directly applied to observational datasets, making them well suited to cases where interior Earth signals remain poorly characterized. We therefore view BSS and ML/DL approaches as complementary, rather than competing, and suggest that systematic benchmarks between them represent a promising avenue for future work.

7 APPLICATION TO GEOPHYSICAL SIGNAL DETECTION IN GRACE TIME SERIES.

7.1 Context

Since 2002, the GRACE and GRACE-FO satellite missions have enabled the monitoring of Earth's time-variable gravity field at a global scale, with a data gap of approximately seven months between the end of GRACE in June 2017 and the start of GRACE-FO in 2018 (Kornfeld et al., 2019; Yi & Sneeuw, 2021). Depending on the processing center and the solution type, gravity field models are released at either ten-day or monthly intervals. For simplicity, we refer to both missions collectively as GRACE in the remainder of this paper.

GRACE data have been instrumental in a wide range of applications, including the monitoring of groundwater storage variations (Awange et al., 2008; Rodell et al., 2009; Syed et al., 2005), ice mass loss (Chen et al., 2007; Matsuo & Heki, 2010; Ramillien et al., 2006), and ocean mass redistribution linked to large-scale circulation and sea level changes (Chen et al., 2020; Delforge et al., 2022; Yu et al., 2018). In terms of solid Earth processes, GRACE has proven capable of detecting mass redistribution associated with major earthquakes (Han et al., 2006; Heki & Matsuo, 2010; Wang et al., 2012). To date, however, only two types of endogenous signals –glacial isostatic adjustment and large earthquakes – have been clearly identified in GRACE data.

Before presenting the analysis of GRACE observations, it is important to recall the role of the synthetic experiments discussed in Section 4. These experiments were not intended to reproduce the full complexity of endogenous or climate signals, but rather to provide a controlled framework in which the performance and limitations of BSS techniques can be systematically assessed. They showed, in particular, under which conditions detection and characterization of interior signals is feasible, how noise levels affect retrieval, and how the number of sources influences separation quality.

The analysis of real GRACE data in this section should therefore be read in light of these benchmarks: while the true underlying signals are not known, the synthetic tests provide guidance on the expected reliability of the methods and on the types of limitations that must be kept in mind when interpreting the results.

We use data from the Gravity Recovery and Climate Experiment (GRACE) and its successor mission GRACE Follow-On (GRACE-FO) to evaluate how signals can be detected in geodetic time series using PCA. Most GRACE-based studies focus on specific regional or continental – scale phenomena, such as major earthquakes, ice sheets, or particular watersheds. Some research extends to global-scale phenomena – for instance, Rodell et al. (2018) and Tapley et al. (2019) analyzed linear trends in major watersheds and glaciers. However, only a few studies have attempted blind source separation to identify and separate sources without prior assumptions (de Viron et al., 2006; Delforge et al., 2022; Long et al., 2017).

In this work, we screen the entire GRACE dataset globally by applying PCA-based blind source separation at each location on the Earth's surface. Additionally, we examine all earthquakes with magnitudes above 6.5 from the ISC catalogue of source mechanisms (International Seismological Centre, 2024), analyzing areas centered on the epicenters with the number of time series included increasing according to the earthquake magnitude.

7.2 Data preparation

We use Equivalent Water Height data from two GRACE products: the JPL Mascon solution (NASA Jet Propulsion Laboratory (JPL) Tellus, 2018) and the GRGS gravity field maps (Lemoine et al., 2022). Prior to any analysis, we remove trends, as well as seasonal and semi-annual signals.

The trend and seasonal terms are estimated independently for each time series by least-squares adjustment of

$$d(t) = \alpha + \beta\cos(2\pi t) + \gamma\sin(2\pi t) + \delta\cos(4\pi t) + \epsilon\sin(4\pi t) + \zeta\,(t - \bar{t}), \quad (9)$$

and the analysis is carried out on the residuals. Because the same linear operator is applied to every series, this step commutes with the mixing: writing $\mathbf{D} = \mathbf{AS}$ and denoting by $\mathbf{P}$ the projector onto the orthogonal complement of the model subspace, the residuals are $\mathbf{DP} = \mathbf{A}(\mathbf{SP})$, so that the mixing matrix, which is the quantity the separation step must recover, is left unchanged. Adjusting the coefficients station by station rather than globally also removes the spatial modulation of the periodic terms, so that no residual coherent seasonal component survives. Conversely, any part of a target signal projecting onto these six functions is removed as well; for a step-like transient this reduces the recovered amplitude but preserves the discontinuity itself, which cannot be represented within a six-dimensional space spanned by annual harmonics and a ramp.

The GRACE time series are then interpolated onto a regular polyhedron grid composed of 16,002 equal-area faces, generated using the icosahedron tool by (Zechmann, 2019). This resampling ensures a uniform spatial coverage over the sphere. Using the original regularly gridded data would bias the analysis by overrepresenting gravity anomalies near the poles.

7.3 Data mining using PCA

For each of the 16,002 vertices on our grid, we identify the 25 nearest vertices, covering an area of approximately 900 × 900 km², and apply Principal Component Analysis (PCA) to the corresponding time series. We retain the first five principal components (PCs), each representing a distinct mode of variability.

For each PC (i.e. temporal mode), we fit the six candidate endogenous signals $Gj(t)$ described in Section 4.2.1 using the following model:

$$D_\ell(t) = \alpha + \beta G_j(t), j = 1, ..., 5 \tag{10}$$

We then selected the signal that provided the best least-squares fit, i.e., the smallest sum of residuals across the 25 time series. Using this best-fitting signal, we next estimated its spatial amplitude over the 25 stations with the same least-squares approach, in order to reconstruct a localized representation of the signal.

We discard a mode if the fitted signal captures less than 50% of the variance of the original 25 time series. Since endogenous signals are not expected to appear uniformly across the globe, we also project the global GRACE dataset onto each PC. We retain a mode only if the median explained variance across the 25 local series exceeds the 95th percentile of explained variances obtained when projecting the same signal onto random time series from all other locations. This ensures that the signal is not only well captured locally, but also statistically significant relative to global variability patterns.

A mode satisfying both criteria is considered significant. Figure 7 displays the grid vertices where at least one of the five modes was found significant: blue for the GRGS model, red for JPL, and green if significant modes appear in both models.

The regions identified by this screening correspond to groundwater, ice, and solid Earth mass changes. Most of the clusters correspond to signatures already published in previous GRACE data analysis studies.

We then reapply PCA to each cluster identified on the map, i.e. on the set of time series from locations that belong to a given cluster. Figure 8 presents the PCA results for the cluster detected in Greenland using the GRGS solution. This example illustrates PCA's capability to separate distinct dynamical regimes without prior assumptions about regions with differing ice flow patterns.

Mode 1 (Figures 8 panels 1.a–1.d) highlights the southeast region, showing a short mass gain in 2002–2003, followed by a decline from 2004 to 2012 that intensifies around 2012, then a renewed increase. Since trends and seasonal oscillations were removed and no post-glacial adjustment correction was applied, this mode corresponds to the southeast zone described by (Velicogna et al., 2020).

Mode 2 (Figures 8 panels 2.a–2.d) captures an increase in western Greenland until 2008, followed by a gradual decline until 2016. This mode aligns with the northwest and southwest zones identified by (Velicogna et al., 2020), with stronger representation in the southwest.

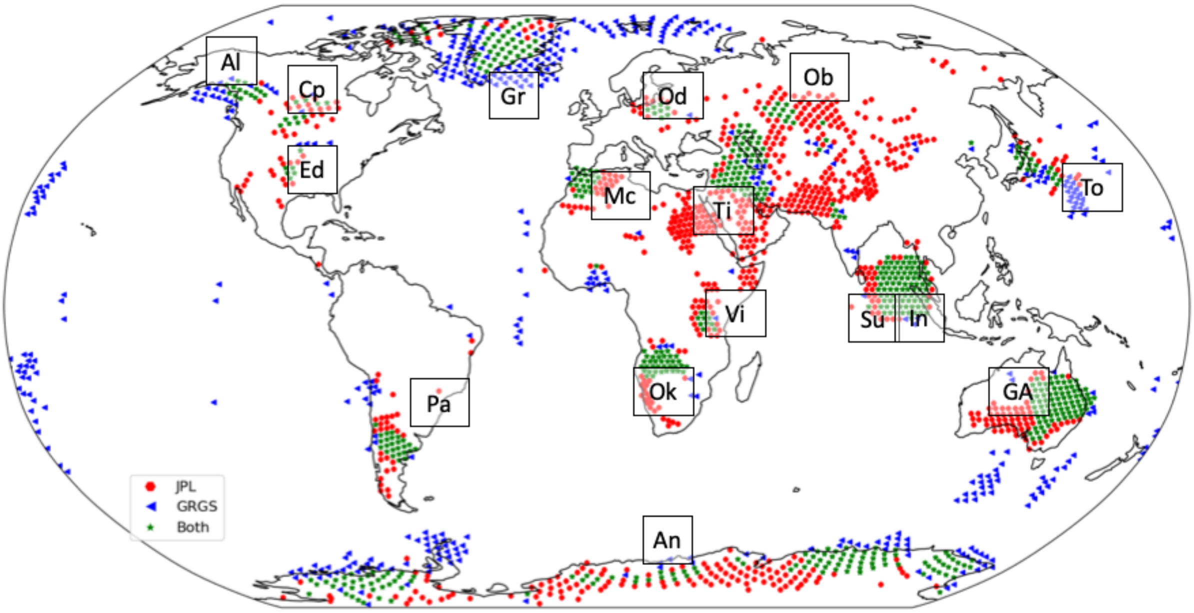

Figure 7. Zones where the retrieved signal appears significant according to the selected criteria. In red, using the GRGS GRACE time series, in blue the Mascon JPL ones, and in green, the zones where both GRACE solutions agree. Among the clusters found, some correspond to previously published signals: hydrological variations in the Southern US High Plains and Edwards-Trinity aquifers (Ed) (Scanlon et al., 2021), the Canadian Prairies (Cp) (Fatolazadeh & Goïta, 2021), Morocco (Mo) (Ouatiki et al., 2022), Lake Victoria (Vi) (Seka et al., 2022), as well as the Okavango-Zambezi (Ok) (Hassan & Jin, 2016), Australian Great Artesian and Murray-Darling (GA) (Yan et al., 2017), Paraná (Pa) (Cornero et al., 2021; Ndehedehe & Ferreira, 2020), Ob-Yenisei-Lena (Ob) (Lin et al., 2022), Tigris-Euphrates (Ti)(Othman et al., 2022; Rateb & Kuo, 2019), and Oder-Vistula (OD) (Sliwińska et al., 2019) river basins. We also detect ice mass changes in Greenland (Gr), Antarctica (An)(Velicogna et al., 2020), and Alaska (Al) (Ciracì et al., 2020). Finally, solid Earth signals related to the 2004 Mw 9.2 Sumatra (Su) (Han et al., 2006), 2011 Mw 9.1 Tohoku-Oki (To) (Han et al., 2014; Wang et al., 2012) megathrust earthquakes, and the 2012 Mw 8.6 strike-slip Indian Ocean event (In) (Han et al., 2015) are recovered.

Finally, mode 3 (Figures 8 3.a–3.d) reflects dynamics in the southwest and especially northeast Greenland, with decreases observed between 2002–2005 and 2012–2014. This mode also captures similar patterns in other regions, for instance, in South America.

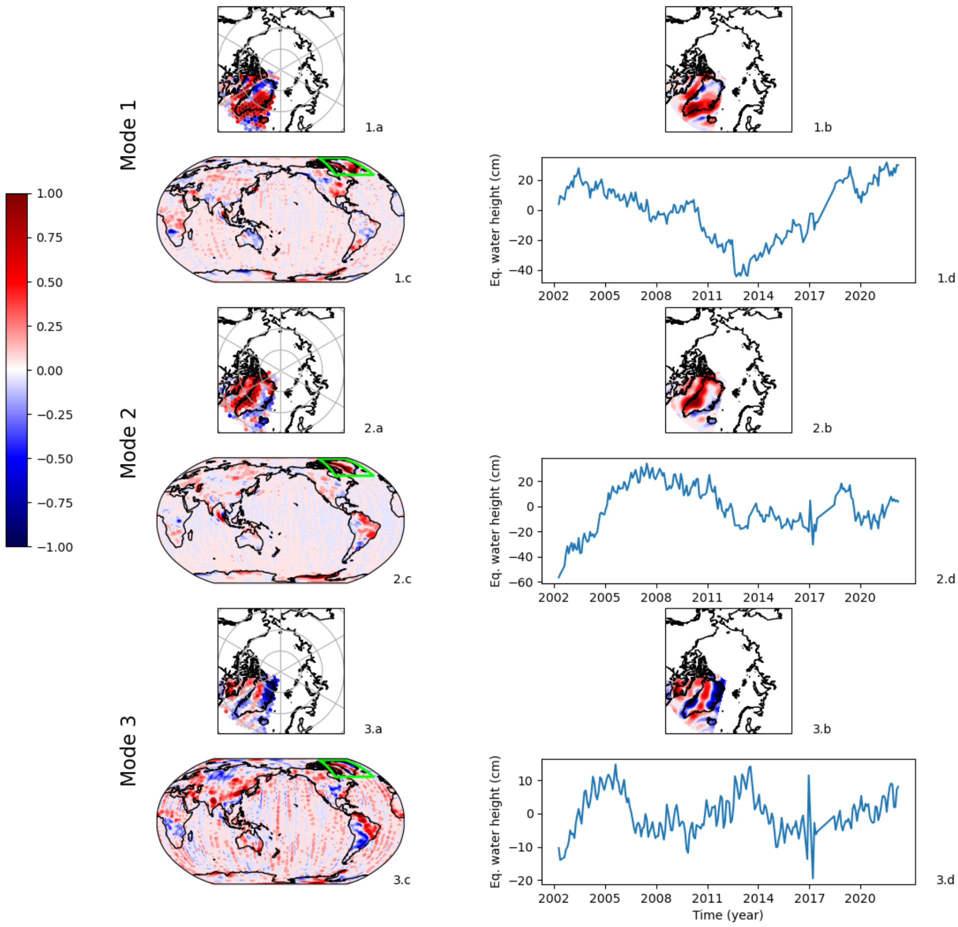

Figure 8. The first, second, and third PCA modes for Greenland in the GRGS GRACE time series. For each mode: (a) Top-left map shows the cluster on which PCA was performed. (b) Top-right map displays the projection of the data onto the principal component (PC) within the cluster area. (c) Bottom-left map shows the global projection of the data onto the same PC. (d) Bottom-right panel presents the time series of the PC. Within this region, the first, second, and third modes explain 23.3%, 17.5%, and 7.8% of the variance, respectively. All maps are normalized to a maximum of 1 so that the PC time series fully captures the amplitude. Blue areas indicate locations evolving in opposition to the PC pattern.

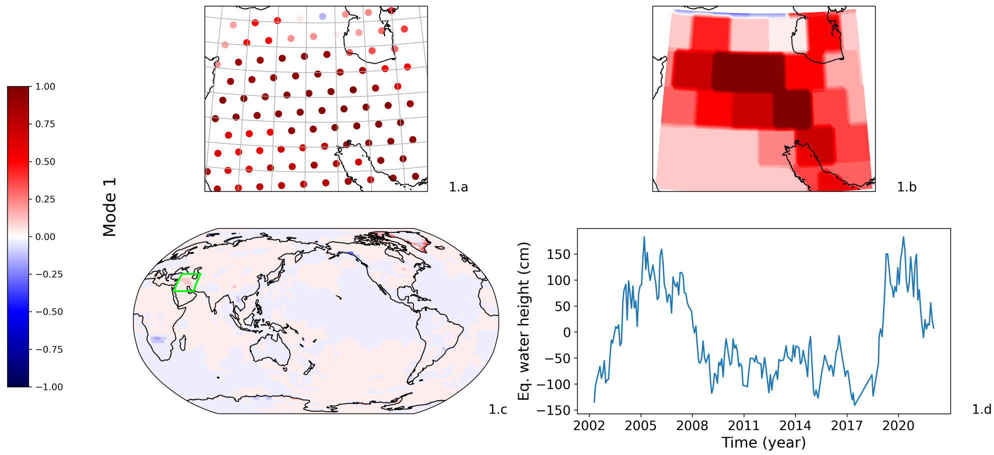

Figure 9. Same as Figure 8, for the first mode in the Tigris-Euphrates watershed capturing 49.3% of the variance of the JPL Mascon GRACE data.

Figure 9 illustrates the PCA for the Tigris-Euphrates watershed and recovers the 2008-2019 drought (Othman et al., 2022).

As a final example, Figure 10 presents the first two principal components (PCs) identified around Sumatra. The first PC captures the co-seismic signal of the 2004 M_w 9.2 Sumatra-Andaman earthquake (Han et al., 2006; Panet et al., 2007), while the second isolates the 2012 Mw 8.6 and 8.2 strike-slip events in the Indian Ocean (Diament et al., 2020; Han et al., 2015). This second component contrasts these events with the larger 2004 Mw 9.2 and 2005 Mw 8.7 Nias earthquakes.

In conclusion, PCA successfully separated distinct geophysical (both climatic and endogenous) signals across different regions of the globe without any prior information. Although no previously unknown signatures were identified, these results demonstrate PCA's capacity to automatically detect and isolate meaningful geophysical phenomena. For example, the method differentiated the effects of the 2004 and 2012 megathrust and strike-slip earthquakes, as well as spatial patterns of ice mass changes in Greenland. The detection test is conditioned by the set of endogenous functions used, which was chosen based on established signal models. Alternative or expanded sets could shift detection sensitivity or facilitate the recovery of other signal types.

7.4 Earthquake detection

As a second test on real data, we applied Principal Component Analysis (PCA) to regions surrounding each earthquake epicenter, using the ISC catalogue of source mechanisms (International Seismological Centre, 2024; Lentas, 2017; Lentas et al., 2019). PCA was selected because, except for the

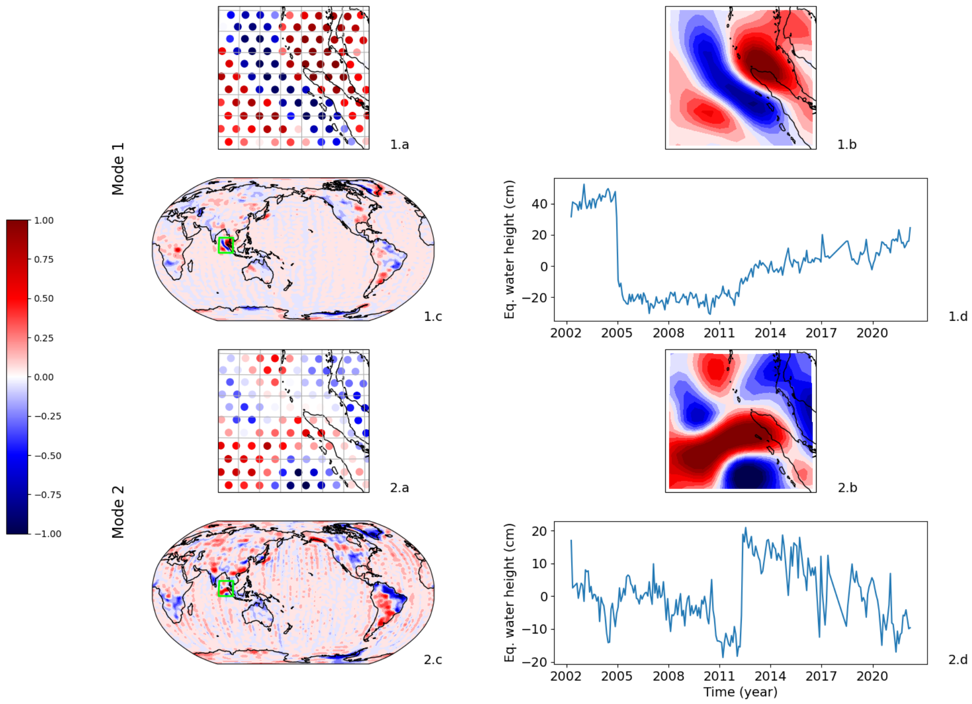

Figure 10. Same as figure 8, for the first and second modes in northern Sumatra, capturing 49.1 and 7.6% of the variance of the GRGS GRACE data. The first mode extracts the signature of the 2004 megathrust Sumatra earthquake, while the second component shows the effect of the 2012 strike-slip Indian Ocean event.

largest events, earthquake-induced signals contribute far less to the total variance than climate-related components. Our analysis included 767 earthquakes occurring between 2004 and 2019, all with moment magnitudes (Mw) greater than 6.5 and for which Global Centroid Moment Tensor solutions are available. The threshold magnitude of 6.5 was chosen because it corresponds to a rupture surface of approximately 200–400 km², which is comparable to the spatial resolution of a single GRACE pixel.

GRACE JPL data were interpolated onto an icosahedral grid composed of 36,002 points. The size of the region used for each PCA was scaled with the earthquake magnitude: from $880 \times 880\,\mathrm{km}^2$ (55 points) for Mw 6.5 events to $1,800 \times 1,800\,\mathrm{km}^2$ (221 points) for Mw 9.0 events.

For each event, we estimated the theoretical co-seismic change in Equivalent Water Height (EWH) by first computing the co-seismic change in gravitational potential using the method of (Okubo, 1992), based on both sets of earthquake parameters. The potential change was expanded into spherical harmonic coefficients, adjusted with load Love numbers to derive the equivalent surface mass distribution, synthesized onto a regular grid, and finally converted to equivalent water height (EWH). While more sophisticated modeling techniques are available (Wang et al., 2006), our goal here was to assess whether the observed gravity signature aligns with theoretical expectations from seismic parameters; high precision was not required.

The temporal evolution of the expected signal was modeled using the following function:

$$S(t) = a + bH(t - t_0) + c\,\mathrm{slope}(t > t_0) + d\,\mathrm{slope}(t < t_0)$$

where $H(t - t_0)$ denotes the Heaviside function, equal to 0 for $t < t_0$ and 1 for $t \geq t_0$; $\mathrm{slope}(t > t_0)$ represents a linear trend starting at 0 when $t = t_0$, while $\mathrm{slope}(t < t_0)$ denotes a linear trend ending at 0 at $t = t_0$.

We applied PCA – previously identified as the most effective detection method in our synthetic experiments – to the GRACE EWH data within each region of interest. Seasonal components and linear trends were removed using a least-squares fitting approach.

Next, we computed the space-time correlation between each of the first five principal components (PCs) obtained from the GRACE data and a synthetic signal constructed as the Okubo-modeled spatial signature multiplied by the Heaviside temporal component described above. Only modes for which the fitted Heaviside function captures at least 25% of the total variance of the associated principal component were retained for further analysis.

To evaluate the statistical significance of each detection, we assume as a null hypothesis H_0 that there is no endogenous signal related to the earthquake, so that the correlations obtained at locations far from the epicenter represent the behavior under H_0. We randomly selected 1,000 locations on the Earth's surface, each at least 5,000 km away from the earthquake epicenter, and computed the same correlations for the first five PCs at each location. Let T_{eq} denote the maximum correlation in the earthquake region and T_i the maximum correlation at the i-th random location. We define the detection statistic as the empirical p-value

$$p = \frac{1}{1000} \sum_{i=1}^{1000} \mathbf{1}\{T_i \geq T_{\mathrm{eq}}\},$$

that is, the proportion of random locations where the highest correlation equals or exceeds the maximum correlation observed in the earthquake region. This quantity estimates the probability, under H_0, of obtaining a maximum correlation at least as large as T_{eq}, and therefore provides an empirical p-value for the detection.

The results for the five events with magnitudes greater than 8.6 are presented in Table 3. Only the large Nias event exhibits a p-value greater than 5%, indicating that the detection of this event was not conclusive. While the other events are formally detected, the correlation between the GRACE

Table 3. Results for the earthquakes of magnitude larger than 8.6. The $p-$value is the proportion of random locations having a correlation with the reconstructed signal as large or larger than the one of the event.

Location	time	M	Correlation	$p-$value
Sumatra–Andaman	2004/12/26	9.0	0.07	0.035
Nias–Simeulue	2005/03/28	8.6	0.055	0.069
Chile	2010/02/27	8.8	0.086	0.001
Tohoku	2011/03/11	9.0	0.140	0.001
Sumatra/Indian ocean	2012/04/11	8.6	0.162	0.007

signal and the synthetic model remains low – consistent with the results obtained in the synthetic tests. However, given the extreme magnitudes of these events, higher correlations could have been expected. The first event occurred very early in the GRACE time series, complicating its detection.

Across the full set of events, we consider an earthquake as detected in the GRACE data if its p-value falls below a given threshold – 5% or 1% – corresponding to 95% and 99% confidence levels, respectively. The detection rate exceeds the expected false detection level: 279 earthquakes (30%) are detected with 95% significance, and 83 (8.7%) with 99% significance. However, the corresponding correlation coefficients remain low. At the 5% threshold, the mean correlation is 0.15 (standard deviation: 0.10), and at the 1% threshold, it rises to 0.20 (standard deviation: 0.11). Under the null hypothesis, the expected number of detections at the locations tested would be 7.7 at the 99% level, against 83 observed. The null expectation accounts for the multiplicity of tested locations and therefore quantifies the number of detections attributable to the selection procedure alone; the observed excess cannot be explained on this basis).

To assess which earthquake parameters most strongly influence detection, we applied a Gradient Boosting Classifier (Friedman, 2002). This ensemble method constructs a series of weak classifiers, optimizing them to reduce detection errors at each iteration. One key output is a feature importance ranking, which quantifies how much each input variable contributes to the decision process across all trees. However, this method does not identify which specific values of a parameter favor detection – it only reveals how informative the parameter is in partitioning the data.

Applied to our dataset, the most influential features for successful detection were the rake, the strike, and the gravity signal amplitude estimated using the Okubo approach. These three parameters ranked higher than event magnitude, both at the 95% and 99% significance levels. The influence of rake and amplitude is expected, since vertical mass displacement is a key factor in generating a detectable gravity signal. The importance of strike is consistent with previous findings by (de Viron et al., 2008), who attributed this effect to the anisotropic spatial structure of GRACE noise, particularly along meridional stripes.

To evaluate the quality of the detection process, we randomly split the dataset into training and testing subsets. The classifier was trained on the training set using earthquake parameters and their detection outcomes, and evaluated on the test set. This procedure was repeated 25,000 times to account for variability due to sample partitioning, and a confusion matrix was computed at each iteration. On average, when trained on detections at the 99% significance level, the classifier achieved an accuracy of 77% (70% for 95%), with a missed detection rate of 13% (14% for 95%) and a false positive rate of 33% (45% for 95%).

These findings suggest that the detection at the 99% significance level is trustworthy. The scores of the classification experiment indicate that performance depends primarily on earthquake parameters, and the variables identified as most influential by the Gradient Booster Classifier are consistent with the underlying physical mechanisms.

Finally, this analysis based on the ISC catalogue reinforces previous conclusions: blind source separation techniques such as PCA are highly effective for identifying subtle signals in complex datasets. However, the recovered signals often lack precision, and caution must be exercised before using them for detailed geophysical interpretation.

8 DISCUSSION

In this study, we assessed the ability of Blind Source Separation (BSS) methods to detect and isolate endogenous signals in space-based gravity observations. Our goal was not to reconstruct precise endogenous fields, but to evaluate whether data-driven techniques could autonomously identify meaningful signals without prior assumptions — a deliberately conservative perspective favouring statistical detectability over physical modelling.

A key outcome is the distinction between detection and interpretability. We defined detection operationally: a signal was deemed detected when the maximum correlation between a retrieved mode and the true signal exceeded the 95th percentile of the null distribution, providing reasonable confidence that it was genuinely captured. This does not, however, guarantee a reliable proxy for the underlying process, so we added an interpretability criterion (correlation $\geq$0.8). That many detections fail this threshold underscores the risk of over-interpreting significant but poorly reconstructed signals.

Among the seven methods tested, only PCA, FastICA and Isomap achieved consistently highest detection rates. PCA performed best at extreme endogenous-to-climate ratios, FICA in intermediate regimes, and Isomap occasionally matched PCA without leading. This ranking reflects the compatibility between each method's assumptions and the mixture structure: methods imposing localisation, purity or positivity are biased by construction, while among the rest, second-order moments (PCA) are more robustly estimated than higher-order or local statistics. The PCA/FICA crossover tracks the eigenvalue spectrum separation rather than the signal ratio itself.

Larger station networks improved separation, especially where endogenous and climate signals compete most. Conversely, endogenous signals only affecting a small subset of a large network, constitute an unfavorable regime, which our study do not sample in details. Incoherent noise degraded performance most severely in these same regimes (losses up to 0.47 at R0.25) — precisely where realistic, heterogeneous noise makes BSS most fragile.

The synthetic sources (steps, relaxations, oscillations) were kept simple, but since BSS relies on spatio-temporal correlations rather than functional form, added complexity would likely reinforce rather than change our conclusions, given that separation is already difficult under tested conditions.

A more fundamental assumption is spatial stationarity ($D = AS$, with time-independent mixing matrix A). Propagating sources fall outside this framework and are instead decomposed into stationary components (typically quadrature pairs), preserving the signal but losing its one-to-one correspondence with a physical source — acceptable for temporally stable internal sources, questionable for propagating surface processes. Convolutive extensions are left to future work.

Missing data and heterogeneous station geometry introduce no new failure modes: no tested method uses station coordinates or temporal ordering, so what matters is each source's variance fraction, already probed via network size and mixing. Common gaps (as in GRACE) simply shorten the record; uneven gaps require infilling, which can itself introduce a spurious coherent component, a pre-processing artefact reinforcing the need for independent validation of any detection.

A complementary deep-learning experiment showed that a simple network can match or exceed BSS in very noisy, weak-signal regimes, but fails to give stable, interpretable results with multiple sources, losing efficiency relative to PCA/ICA as their number grows. The two approaches appear complementary, with systematic benchmarking a promising avenue.

Applying PCA to real GRACE data, after removing trends and seasonal terms (a deterministic step distinct from blind separation, since these dominant signals have known origins), a global analysis recovered most previously identified regions, confirming PCA's value as a fast, assumption-free screening tool. Applied to Equivalent Water Height series for 767 earthquakes (M6.5), it detected a significant fraction of events (nearly 30% at 95% significance level, 9% at 99%), including several well below M8.5 — challenging the view that GRACE detects only the largest earthquakes, and illustrating BSS's value for rapid candidate screening ahead of detailed modelling. Nevertheless, even for largest earthquakes, correlation between retrieved and modeled gravity signatures remains low.

Future work could combine BSS with physical modelling, extend to multi-sensor datasets, exploit longer time series, and pursue systematic integration of BSS and machine learning with rigorous uncertainty quantification to bridge data-driven and physically grounded interpretation.

9 CONCLUSION

We have investigated the ability of Blind Source Separation (BSS) methods to detect and isolate endogenous signals in satellite gravity data, through an extensive set of synthetic experiments spanning signal-to-noise ratios, source types, mixing conditions, and network sizes. Our results establish a clear distinction between statistical detectability and geophysical interpretability: while PCA, FastICA and Isomap can reliably detect weak signals even in the presence of stronger climate-related components, confident physical interpretation demands a high standard of reconstruction fidelity, one often not met even when detection is statistically significant.

Applications to real GRACE data confirm the practical value of this approach: a global PCA analysis recovered most previously identified regions of coherent mass change, and a systematic search over 767 earthquakes ($M \geq 6.5$) revealed statistically significant gravity signals for a substantial fraction of events, including several well below magnitude 8.5.

These findings support the use of BSS, and PCA in particular, as a fast, assumption-free screening tool for identifying candidate endogenous signals in complex geodetic datasets — one that should be paired with physically based modelling and independent validation rather than used as a standalone interpretive method. Extending this framework to longer time series, multi-sensor datasets, and hybrid BSS/machine-learning approaches offers a promising path toward more reliable and interpretable detection of subtle endogenous signals.

10 DATA AND SOFTWARE AVAILABILITY

The GRACE data are public domain on `https://podaac.jpl.nasa.gov/` for the JPL mascon solution, and on `https://grace.obs-mip.fr/` for the GRGS solution. The climate indices time series are public domains on the Physical Sciences Laboratory `https://psl.noaa.gov/data/climateindices/list/`. To ensure reproducibility and facilitate further research, we provide four Python-based tools developed for this study:

- A source separation library implementing the seven blind source separation (BSS) methods evaluated in this work, including their mathematical foundations and preprocessing steps.
- A synthetic time-series generator reproducing the simulated data used in our experiments, with customizable parameters for source characteristics and noise levels.

- A neural network framework for source separation, including the trained model architecture and a testing pipeline on benchmark datasets.
- A gravity effect computation module based on Okubo's approach, enabling the calculation of seismic-induced gravity changes for synthetic or real datasets.

All codes are publicly available under open-source licenses at `https://github.com/odeviron/BSS`.

ACKNOWLEDGMENTS

This research was supported by CNES as an application of the GRACE gravity mission. The authors thank Dmitry Storchak for his guidance regarding the ISC catalogs. We sincerely thank the editor Duncan Agnew, the second editor Bert Vermeersen, and three anonymous revewiers for their help in making the manuscript more rigorous and understandable.

References

Abdi, H., 2003. Factor rotations in factor analyses, in Encyclopedia for Research Methods for the Social Sciences, edited by M. S. Lewis-Beck, A. Bryman, & T. F. Liao, pp. 792–795, Sage Publications, Thousand Oaks (CA).

Agnew, D. C., 1992. The time-domain behavior of power-law noises, *Geophys. Res. Lett.*, **19**(4), 333–336.

Agnew, D. C., 2013. Realistic simulations of geodetic network data: The Fakenet package, *Seismol. Res. Lett.*, **84**(3), 426–432.

Alpala, R., Alpala, J., Rosell, P. A., Euillades, L. D., Euillades, P. A., & Battaglia, M., 2025. Satellite geodesy reveals shallow, transient magma intrusions at Sotará Volcano, Colombia, *J. Geophys. Res.-Sol. Ea.*, **130**(12), e2025JB031856.

Altamimi, Z., Rebischung, P., Métivier, L., & Collilieux, X., 2016. ITRF2014: A new release of the International Terrestrial Reference Frame modeling nonlinear station motions, *J. Geophys. Res.-Sol. Ea.*, **121**(8), 6109–6131.

Awange, J. L., Sharifi, M. A., Ogonda, G., Wickert, J., Grafarend, E. W., & Omulo, M. A., 2008. The falling Lake Victoria water level: GRACE, TRIMM and CHAMP satellite analysis of the lake basin, *Water Resour. Manag.*, **22**(7), 775–796.

Ballu, V., Gravelle, M., Wöppelmann, G., de Viron, O., Rebischung, P., Becker, M., & Sakic, P., 2019. Vertical land motion in the Southwest and Central Pacific from available GNSS solutions and implications for relative sea levels, *Geophys. J. Int.*, **218**(3), 1537–1551.

Basak, J., Sudarshan, A., Trivedi, D., & Santhanam, M. S., 2004. Weather data mining using Independent Component Analysis, *J. Mach. Learn. Res.*, **5**, 239–253.

Bekaert, D. P. S., Segall, P., Wright, T. J., & Hooper, A. J., 2016. A network inversion filter combining gnss and insar for tectonic slip modeling, *J. Geophys. Res.-Sol. Ea.*, **121**(3), 2069–2086.

Bevis, M. & Brown, A., 2014. Trajectory models and reference frames for crustal motion geodesy, *J. Geod.*, **88**, 283–311.

Boergens, E., Rangelova, E., Sideris, M., & Kusche, J., 2014. Assessment of the capabilities of the temporal and spatiotemporal ICA method for geophysical signal separation in GRACE data, *J. Geophys. Res.-Sol. Ea.*, **119**(5), 4429–4447.

Borg, I. & Groenen, P. J. F., 2005. *Modern multidimensional scaling: theory and applications*, Springer, 2nd edn.

Chao, B. F. & Liau, J. R., 2019. Gravity changes due to lLarge earthquakes detected in GRACE satellite data via Empirical Orthogonal Function analysis, *J. Geophys. Res.-Sol. Ea.*, **124**(3), 3024–3035.

Chen, J., Tapley, B., Wilson, C., Cazenave, A., Seo, K., & Kim, J., 2020. Global ocean mass change from GRACE and GRACE Follow-On and altimeter and Argo measurements, *Geophys. Res. Lett.*, **47**(22).

Chen, J. L., Wilson, C. R., Tapley, B. D., Blankenship, D. D., & Ivins, E. R., 2007. Patagonia Icefield melting observed by Gravity Recovery and Climate Experiment (GRACE), *Geophys. Res. Lett.*, **34**(22), L22501.

Ciracì, E., Velicogna, I., & Swenson, S., 2020. Continuity of the mass loss of the world's glaciers and ice caps from the grace and grace follow-on missions, *Geophys. Res. Lett.*, **47**(9).

Comon, P., 1994. Independent Component Analysis, A New Concept?, *Signal Process.*, **36**(3), 287–314.

Cornero, C., Pereira, A., Matos, A. C. O. C., Pacino, M. C., & Blitzkow, D., 2021. Monitoreo de la variación del almacenamiento de agua en la cuenca del Medio y Bajo Paraná a partir de datos GRACE, GRACE FO, TRMM y GLDAS, *Rev. teledetec.*, (58), 53.

Crossley, D., de Linage, C., Hinderer, J., Boy, J.-P., & Famiglietti, J., 2012. A comparison of the gravity field over Central Europe from superconducting gravimeters, GRACE and global hydrological models, using EOF analysis, *Geophys. J. Int.*, **189**(2), 877–897.

de Viron, O., Panet, I., & Diament, M., 2006. Extracting low frequency climate signal from GRACE data, *eEarth*, **1**(1), 9–14.

de Viron, O., Panet, I., Mikhailov, V., Van Camp, M., & Diament, M., 2008. Retrieving earthquake signature in GRACE gravity solutions, *Geophys. J. Int.*, **174**(1), 14–20.

Delforge, D., de Viron, O., Durand, F., & Dehant, V., 2022. The global patterns of interannual and intraseasonal mass variations in the oceans from GRACE and GRACE Follow-On records, *Remote Sens.*, **14**(8), 1861.

Diament, M., Mikhailov, V., & Timoshkina, E., 2020. Joint inversion of GPS and high-resolution GRACE gravity data for the 2012 Wharton basin earthquakes, *J. Geodyn.*, **136**, 101722.

Dmitrieva, K., Segall, P., & DeMets, C., 2015. Network-based estimation of time-dependent noise in gps position time series, *J. Geod.*, **89**(7), 591–606.

Fabbri, O., Raimbourg, H., & Leclère, H., 2024. Fluids, faulting and earthquakes in the brittle crust: recent advances and new challenges, *C.R. Geosci.*, **356**(S2), 423–466.

Fatolazadeh, F. & Goïta, K., 2021. Mapping terrestrial water storage changes in Canada using GRACE and GRACE-FO, *Sci. Total Environ.*, **779**, 146435.

Forootan, E. & Kusche, J., 2012. Separation of global time-variable gravity signals into maximally independent components, *J. Geod.*, **86**(7), 477–497.

Forootan, E., Awange, J., Kusche, J., Heck, B., & Eicker, A., 2012. Independent patterns of water mass anomalies over Australia from satellite data and models, *Remote Sens. Environ.*, **124**, 427–443.

Fraino, P. E., 2023. Using principal component analysis to explore multi-variable relationships, *Nat. Rev. Earth Environ.*, **4**, 294.

Frappart, F., Ramillien, G., Leblanc, M., Tweed, S., Bonnet, M.-P., & Maisongrande, P., 2011. An independent component analysis filtering approach for estimating continental hydrology in the GRACE gravity data, *Remote Sens. Environ.*, **115**(1), 187–204.

Friedman, J., 2002. Stochastic Gradient Boosting, *Comput. Stat. Data Anal.*, **38**, 367–378.

Gobron, K., Rebischung, P., Van Camp, M., Demoulin, A., & de Viron, O., 2021. Influence of aperiodic non-tidal atmospheric and oceanic loading deformations on the stochastic properties of global GNSS vertical land motion time series, *J. Geophys. Res.-Sol. Ea.*, **126**(9).

Han, S., Sauber, J., & Pollitz, F., 2014. Broadscale postseismic gravity change following the 2011 Tohoku-Oki earthquake and implication for deformation by viscoelastic relaxation and afterslip, *Geophys. Res. Lett.*, **41**(16), 5797–5805.

Han, S., Sauber, J., & Pollitz, F., 2015. Coseismic compression/dilatation and viscoelastic uplift/subsidence following the 2012 Indian Ocean earthquakes quantified from satellite gravity observations, *Geophys. Res. Lett.*, **42**(10), 3764–3772.

Han, S.-C., Shum, C. K., Bevis, M., Ji, C., & Kuo, C.-Y., 2006. Crustal dilatation observed by GRACE after the 2004 Sumatra-Andaman earthquake, *Science*, **313**(5787), 658–662.

Hanjiang, W., Guangbin, Z., Pengfei, C., & Xiaotao, C., 2009. EOF Analysis on the variations of continental water storage from GRACE in China, *Int. Assoc. Geod. Symp.*, **133**, 315–321.

Hassan, A. & Jin, S., 2016. Water storage changes and balances in Africa observed by GRACE and hydrologic models, *Geod. Geodyn.*, **7**(1), 39–49.

Heki, K. & Matsuo, K., 2010. Coseismic gravity changes of the 2010 earthquake in central Chile from satellite gravimetry, *Geophys. Res. Lett.*, **37**(24), L24306.

Holme, R. & de Viron, O., 2013. Characterization and implications of intradecadal variations in length of day, *Nature*, **499**(7457), 202 – 204.

Hyvärinen, A. & Oja, E., 1999. Fast Independent Component Analysis, *Neural Comput.*, **11**(4), 821–842.

International Seismological Centre, 2024. International Seismological Centre On-line Bulletin.

Jha, P. K., Schüth, C., & Schirmer, M., 2014. Using Isomap to differentiate between anthropogenic and natural effects on groundwater dynamics in a complex geological setting, *J. Hydrol.*, **519**, 1008–1021.

Jin, S., van Dam, T., & Wdowinski, S., 2013. Observing and understanding the Earth system variations from space geodesy, *J. Geodyn.*, **72**, 1–10.

Kaiser, H., 1958. The varimax criterion for analytic rotation in factor analysis, *Psychometrika*, **23**(3), 187–200.

Kiani Shahvandi, M., Adhikari, S., Dumberry, M., et al., 2024. Contributions of core, mantle and climatological processes to Earth's polar motion, *Nat. Geosci.*, **17**, 705–710.

Kiani Shahvandi, M., Noir, J., Mishra, S., & Soja, B., 2024. Length of day variations explained in a bayesian framework, *Geophys. Res. Let.*, **51**(22), e2024GL111148.

Kornfeld, R. P., Arnold, B. W., Gross, M. A., Dahya, N. T., Klipstein, W. M., Gath, P. F., & Bettadpur, S., 2019. GRACE-FO: The Gravity Recovery and Climate Experiment Follow-On Mission, *J. Spacecr. Rockets*, **56**(3), 931–951.

Kositsky, A. & Avouac, J.-P., 2010. Inverting geodetic time series with a principal component analysis-based inversion method, *J. Geophys. Res.-Sol. Ea.*, **115**(3).

Lawley, D. N. & Maxwell, A. E., 1971. *Factor Analysis as a statistical method*, Butterworths, London, 2nd edn.

Lee, D. D. & Seung, H. S., 1999. Learning the parts of objects by non-negative matrix factorization, *Nature*, **401**(6755), 788–791.

Lee, J.-M., Koenig, A. E., & Giosan, L., 2007. Using non-negative matrix factorization in the "unmixing" of diffuse reflectance spectra, *Mar. Pollut. Bull.*, **54**(9-10), 1520–1533.

Lemoine, J.-M., Balmino, G., Bruinsma, S., Perosanz, F., Marty, J.-C., Loyer, S., Bourgogne, S., Gégout, P., & Biancale, R., 2022. 20 years of Gravity Variations from GRACE, GRACE-FO and SLR data from CNES/GRGS.

Lentas, K., 2017. Towards routine determination of focal mechanisms obtained from first motion P-wave arrivals, *Geophys. J. Int.*, **212**(3), 1665–1686.

Lentas, K., Di Giacomo, D., Harris, J., & Storchak, D. A., 2019. The ISC Bulletin as a comprehensive source of earthquake source mechanisms, *Earth Syst. Sci. Data*, **11**(2), 565–578.

Lin, H., Cheng, X., Zheng, L., Peng, X., Feng, W., & Peng, F., 2022. Recent changes in groundwater and surface water in large Pan-Arctic river basins, *Remote Sens.*, **14**(3), 607.

Liu, J. & Mao, H.-K., 2021. Yi-Gang Xu: the Earth's deep interior holds the key to habitability, *Natl. Sci. Rev.*, **8**(4), nwab018.

Long, D., Pan, Y., Zhou, J., Chen, Y., Hou, X., Hong, Y., Scanlon, B. R., & Longuevergne, L., 2017. Global analysis of spatiotemporal variability in merged total water storage changes using multiple GRACE products and global hydrological models, *Remote Sens. Environ.*, **192**, 198–216.

Magyar, B., Kenyeres, A., Tóth, S., Hajdu, I., & Horváth, R., 2022. Spatial outlier detection on discrete GNSS velocity fields using robust Mahalanobis-distance-based unsupervised classification, *GPS Solut.*, **26**(4), 145.

Mandea, M., Panet, I., Lesur, V., De Viron, O., Diament, M., & Le Mouël, J.-L., 2012. Recent changes of the Earth's core derived from satellite observations of magnetic and gravity fields, *Proc. Natl. Acad. Sci. U. S. A.* , **109**(47), 19129–19133.

Matsuo, K. & Heki, K., 2010. Time-variable ice loss in Asian high mountains from satellite gravimetry, *Earth Planet. Sci. Lett.*, **290**(1-2), 30–36.

Maubant, L., Pathier, E., Daout, S., Radiguet, M., Doin, M., Kazachkina, E., Kostoglodov, V., Cotte, N., & Walpersdorf, A., 2020. Independent Component Analysis and parametric approach for source separation in InSAR time series at regional scale: Application to the 2017–2018 Slow Slip event in Guerrero (Mexico), *J. Geophys. Res.-Sol. Ea.*, **125**(3).

Munekane, H., 2012. Coseismic and early postseismic slips associated with the 2011 off the Pacific coast of Tohoku Earthquake sequence: EOF analysis of GPS kinematic time series, *Earth Planets Space*, **64**(12), 1077–1091.

Murray, J. R., Segall, P., & Cervelli, P. F., 2013. Tremor and slow slip on the cascadia subduction zone: A comparison of two methods for estimating slip distributions, *J. Geophys. Res.-Sol. Ea.*, **118**(5), 2569–2585.

Murtagh, F., 1991. Multilayer perceptrons for classification and regression, *Neurocomputing*, **2**(5), 183–197.

Métivier, L., Rouby, H., Rebischung, P., & Altamimi, Z., 2020. ITRF2014, Earth figure changes, and geocenter velocity: Implications for GIA and recent ice melting, *J. Geophys. Res.-Sol. Ea.*, **125**(2).

NASA Jet Propulsion Laboratory (JPL) Tellus, 2018. JPL GRACE Mascon ocean, ice, and hydrology equivalent water height Release 06 Coastal Resolution Improvement (CRI) Filtered Version 1.0.

Ndehedehe, C. E. & Ferreira, V. G., 2020. Assessing land water storage dynamics over South America, *J. Hydrol.*, **580**, 124339.

Nerem, R. S., Talpe, M., Pilinski, E., Lemoine, F. G., & Chinn, D. S., 2013. Reconstruction of Greenland and Antarctica mass changes prior to the GRACE mission, in EGU General Assembly Conference Abstracts, EGU General Assembly Conference Abstracts, pp. EGU2013–11285.

NOAA Physical Sciences Laboratory, 2009. Climate Indices: monthly atmospheric and ocean time series, `https://psl.noaa.gov/data/climateindices/list/`.

Okubo, S., 1992. Gravity and potential changes due to shear and tensile faults in a half-space, *J. Geophys. Res.-Sol. Ea.*, **97**(B5), 7137–7144.

Othman, A., Abdelrady, A., & Mohamed, A., 2022. Monitoring mass variations in Iraq using time-variable gravity data, *Remote Sens.*, **14**(14), 3346.

Ouatiki, H., Boudhar, A., Leblanc, M., Fakir, Y., & Chehbouni, A., 2022. When climate variability partly compensates for groundwater depletion: an analysis of the GRACE signal in Morocco, *J. Hydrol. Reg. Stud.*, **42**, 101177.

Panet, I., Mikhailov, V., Diament, M., Pollitz, F., King, G., de Viron, O., Holschneider, M., Biancale, R., & Lemoine, J.-M., 2007. Coseismic and post-seismic signatures of the Sumatra 2004 December and 2005 March earthquakes in GRACE satellite gravity, *Geophys. J. Int.*, **171**(1), 177–190.

Panet, I., Narteau, C., Lemoine, J.-M., Bonvalot, S., & Remy, D., 2022. Detecting preseismic signals in GRACE gravity solutions: Application to the 2011 Tohoku Mw 9.0 earthquake, *J. Geophys. Res.-Sol. Ea.*, **127**(8).

Patzelt, F., 2023. colorednoise: A Python package for generating colored noise, https://github.com/felixpatzelt/colorednoise.

Pearson, K., 1901. On lines and planes of closest fit to systems of points in space, *Philos. Mag.*, **2**, 559–572.

Preisendorfer, R. & Mobley, C., 1988. *Principal Component Analysis in meteorology and oceanography*, Developments in atmospheric science, Elsevier.

Ramillien, G., Lombard, A., Cazenave, A., Ivins, E., Llubes, M., Remy, F., & Biancale, R., 2006. Interannual variations of the mass balance of the Antarctica and Greenland ice sheets from GRACE, *Glob. Planet. Change*, **53**(3), 198–208.

Rangelova, E. & Sideris, M., 2008. Contributions of terrestrial and GRACE data to the study of the secular geoid changes in North America, *J. Geodyn.*, **46**(3-5), 131–143.

Rangelova, E., van der Wal, W., Braun, A., Sideris, M., & Wu, P., 2007. Analysis of Gravity Recovery and Climate Experiment time-variable mass redistribution signals over North America by means of principal component analysis, *J. Geophys. Res.- Earth*, **112**(3).

Rateb, A. & Kuo, C.-Y., 2019. Quantifying vertical deformation in the Tigris–Euphrates Basin due to the groundwater abstraction: insights from GRACE and Sentinel-1 satellites, *Water*, **11**(8), 1658.

Reed, W. E. & Levin, H. L., 1981. *Factor Analysis in geology*, Wiley, New York.

Richman, M. B., 1986. Rotation of principal components, *J. Climatol.*, **6**, 293–335.

Riel, B., Simons, M., Agram, P., & Zhan, Z., 2014. Detecting transient signals in geodetic time series using sparse estimation techniques, *J. Geophys. Res.-Sol. Ea.*, **119**(6), 5140–5160.

Rodell, M., Velicogna, I., & Famiglietti, J. S., 2009. Satellite-based estimates of groundwater depletion in India, *Nature*, **460**(7258), 999–1002.

Rodell, M., Famiglietti, J. S., Wiese, D. N., Reager, J. T., Beaudoing, H. K., Landerer, F. W., & Lo, M.-H., 2018. Emerging trends in global freshwater availability, *Nature*, **557**(7707), 651–659.

Rummel, R., 2010. The interdisciplinary role of space geodesy — Revisited, *J. Geodyn.*, **49**(3-4), 112–115.

Saraswati, A. T., de Viron, O., & Mandea, M., 2023. Earth's core variability from magnetic and gravity field observations, *Solid Earth*, **14**(12), 1267–1287.

Savage, J. C., 1988. Principal Component Analysis of geodetically measured deformation in Long Valley Caldera, Eastern California, 1983-1987, *J. Geophys. Res.-Sol. Ea.*, **93**(B11), 13297–13305.

Scanlon, B. R., Rateb, A., Pool, D. R., Sanford, W., Save, H., Sun, A., Long, D., & Fuchs, B., 2021. Effects of climate and irrigation on GRACE-based estimates of water storage changes in major US aquifers, *Environ. Res. Lett.*, **16**(9), 094009.

Scherneck, H.-G., Johansson, J., Vermeer, M., Davis, J., Milne, G., & Mitrovica, J., 2001. BIFROST project: 3-D crustal deformation rates derived from GPS confirm postglacial rebound in Fennoscandia, *Earth Planets Space*, **53**, 703–708.

Schmidt, R., Flechtner, F., Meyer, U., Neumayer, K.-H., Dahle, C., König, R., & Kusche, J., 2008. Hydrological signals observed by the GRACE satellites, *Surv. Geophys.*, **29**(4-5), 319–334.

Schrama, E., Wouters, B., & Lavallée, D., 2007. Signal and noise in Gravity Recovery and Climate Experiment (GRACE) observed surface mass variations, *J. Geophys. Res.-Sol. Ea.*, **112**(8).

Segall, P. & Matthews, M. V., 1997. Time dependent inversion of geodetic data, *J. Geophys. Res.-Sol. Ea.*, **102**(B10), 22391–22409.

Seka, A. M., Zhang, J., Ayele, G. T., Demeke, Y. G., Han, J., & Prodhan, F. A., 2022. Spatio-temporal analysis of water storage variation and temporal correlations in the East Africa lake basins, *J. Hydrol. Reg. Stud.*, **41**, 101094.

Sindoni, G., Pavlis, E. C., Paris, C., Paolozzi, A., & Ciufolini, I., 2016. Effects of Climate Change on Earth's Parameters - An Example of Exabyte-sized System:, in Proceedings of the 1st International

Conference on Complex Information Systems, pp. 131–138, SCITEPRESS - Science and and Technology Publications, Rome, Italy.

Sliwińska, J., Birylo, M., Rzepecka, Z., & Nastula, J., 2019. Analysis of groundwater and total water storage changes in Poland using GRACE observations, in-situ data, and various assimilation and climate models, *Remote Sens.*, **11**(24), 2949.

Spearman, C., 1904. General Intelligence, objectively determined and measured, *Am. J. Psychol.*, **15**(2), 201–292.

Srivastava, N., Hinton, G., Krizhevsky, A., Sutskever, I., & Salakhutdinov, R., 2014. Dropout: a simple way to prevent neural networks from overfitting, *J. Mach. Learn. Res.*, **15**(56), 1929–1958.

Syed, T. H., Famiglietti, J. S., Chen, J., Rodell, M., Seneviratne, S. I., Viterbo, P., & Wilson, C. R., 2005. Total basin discharge for the Amazon and Mississippi River basins from GRACE and a land-atmosphere water balance, *Geophys. Res. Lett.*, **32**(24), L24404.

Tapley, B. D., Watkins, M. M., Flechtner, F., Reigber, C., Bettadpur, S., Rodell, M., Sasgen, I., Famiglietti, J. S., Landerer, F. W., Chambers, D. P., Reager, J. T., Gardner, A. S., Save, H., Ivins, E. R., Swenson, S. C., Boening, C., Dahle, C., Wiese, D. N., Dobslaw, H., Tamisiea, M. E., & Velicogna, I., 2019. Contributions of GRACE to understanding climate change, *Nat. Cli. Change*, **9**(5), 358–369.

Tenenbaum, J. B., de Silva, V., & Langford, J. C., 2000. A global geometric framework for nonlinear dimensionality reduction, *Science*, **290**(5500), 2319–2323.

Theiler, J., Eubank, S., Longtin, A., Galdrikian, B., & Farmer, J. D., 1992. Testing for nonlinearity in time series: the method of surrogate data, *Physica D Nonlinear Phenom.*, **58**(1–4), 77–94.

Timmer, J. & Koenig, M., 1995. On generating power law noise, *Astron. Astrophys.*, **300**, 707–710.

Valty, P., De Viron, O., Panet, I., & Collilieux, X., 2015. Impact of the North Atlantic Oscillation on Southern Europe water distribution: Insights from geodetic data, *Earth Interact.*, **19**(10).

Van Camp, M., de Viron, O., Watlet, A., Meurers, B., Francis, O., & Caudron, C., 2017. Geophysics from terrestrial time-variable gravity measurements, *Rev. Geophys.*, **55**(4), 938–992.

Van Den Dool, H., Saha, S., & Johansson, A., 2000. Empirical orthogonal teleconnections, *J. Clim.*, **13**(8), 1421–1435.

Velicogna, I., Mohajerani, Y., A, G., Landerer, F., Mouginot, J., Noel, B., Rignot, E., Sutterley, T., van den Broeke, M., van Wessem, M., & Wiese, D., 2020. Continuity of ice sheet mass loss in Greenland and Antarctica from the GRACE and GRACE Follow-On missions, *Geophys. Res. Lett.*, **47**(8).

von Storch, H. & Zwiers, F. W., 1999. *Statistical Analysis in Climate Research*, Cambridge University Press, Cambridge, 1st edn.

Wang, L., Shum, C. K., Simons, F. J., Tapley, B., & Dai, C., 2012. Coseismic and postseismic deformation of the 2011 Tohoku-Oki earthquake constrained by GRACE gravimetry, *Geophys. Res. Lett.*, **39**(7), n/a–n/a.

Wang, R., Lorenzo-Martin, F., & Roth, F., 2006. PSGRN/PSCMP – a new code for calculating co- and post-seismic deformation, geoid and gravity changes based on the viscoelastic-gravitational dislocation theory, *Comput. Geosci.*, **32**(4), 527–541.

Wouters, B. & Schrama, E., 2007. Improved accuracy of GRACE gravity solutions through empirical orthogonal function filtering of spherical harmonics, *Geophys. Res. Lett.*, **34**(23).

Xiong, Y., Feng, W., Zhou, X., Kusche, J., Shen, Y., Yang, M., Wang, C., & Zhong, M., 2024. Separation of earthquake and hydrology signals from GRACE satellites data via independent component analysis: a case study in the Sumatra region, *Geophys. J. Int.*, **239**(3), 1597–1616.

Yan, J., Jia, S., Lv, A., Mahmood, R., & Zhu, W., 2017. Analysis of the spatio-temporal variability of terrestrial water storage in the Great Artesian Basin, Australia, *Water Supply*, **17**(2), 324–341.

Yi, S. & Sneeuw, N., 2021. Filling the data gaps within GRACE missions using singular spectrum analysis, *J. Geophys. Res.-Sol. Ea.*, **126**(5).

Yu, Y., Chao, B. F., García-García, D., & Luo, Z., 2018. Variations of the Argentine Gyre observed in the GRACE time-variable gravity and ocean altimetry measurements, *J. Geophys. Res.- Oceans*, **123**(8), 5375–5387.

Zechmann, E., 2019. Make Icosahedron, https://www.mathworks.com/matlabcentral/fileexchange/19169-make-icosahedron.

Zerbini, S., Raicich, F., Errico, M., & Cappello, G., 2013. An EOF and SVD analysis of interannual variability of GPS coordinates, environmental parameters and space gravity data, *J. Geodyn.*, **67**, 111–124.

Ziegler, Y., Vishwakarma, B. D., Brady, A., Chuter, S., Royston, S., Westaway, R. M., & Bamber, J. L., 2022. Can GPS and GRACE data be used to separate past and present-day surface loading in a data-driven approach?, *Geophys. J. Int.*, **232**(2), 884–901.

Appendix A: Global simulation algorithm

```
for L in [8,12,16,20] do                                          ▷ loop on the number of series
  for K in [0,1,2] do                                     ▷ loop on the number of climate sources
    for J in [1,2] do                                ▷ loop on the number of endogenous sources
      for σ in [0.1 , 0.25, 0.5,0.75, 1] do              ▷ loop on the noise standard deviation
        for lr in range(1000) do
          Patterns=random(L,K+J)                                ▷ Geometry patterns of sources
          Geophys=GenerateGeophys(J,len(t))            ▷ Select type and Generate J random ...
                                                           ▷ ... endogenous-like time series
          Climate=SelectClimate(K,len(t))                     ▷ Select K climate time series
          for R in [0.01,0.05,...,2] do           ▷ loop on the endogenous to climate ratio
            PowerLawIndex=random*3-2                                      ▷ Index ∈ [-2,1]
            WhiteNoise=Normal(Mean=0,Var=σ²,len(t))
            PowerLawNoise=σ×PowerLaw(PowerLawIndex,len(t))
            Simul=zeros(len(t),L)
            Simul0=zeros(len(t),L)                           ▷ with no endogenous source
            for k in range(K) do                                          ▷ Climate signals
              D=D+Patterns[:,k]×Climate[k,:]
              Db=Db+Patterns[:,k]×Climate[k,:]
              Sources[:,k]=Patterns[:,k]×Climate[k,:]
            end for
            for j in range(J) do                                       ▷ Endogenous signal)
              D=D+Patterns[:,K+j]×Geophys[j,:]
                                                                  ▷ No endogenous signal
              Sources[:,K+j]=Patterns[:,k]×Geophys[j,:]
            end for
            D=D+PowerLawNoise+WhiteNoise
            Db=Db+PowerLawNoise+WhiteNoise
            for method in [PCA,Varimax,...,Isomap] do
              u,pc,w=method(D,nmode=5)                                                ▷ BSS
              ub,pcb,wb=method(Db,nmode=5)
              for j in range(J) do
                for mode in range(5) do
                  Results=Correlation(u[:,mode]× pc[mode,:],Sources[:,K+j])
                  Resultsb=Correlation(u[:,mode]× pc[mode,:],Sources[:,K+j])
                                           ▷ Simulation parameters and results are saved
                end for
                ...                                               ▷ All the loops are closed
```